Earth and Planetary Science | Volume 03 | Issue 02 | October 2024

Earth and Planetary Science

https://journals.nasspublishing.com/index.php/eps

RESEARCH ARTICLE

2.13 Ga Lawsonite/Barroisite-Bearing E-Morb Signature Metagabbro Associated with Spinel Metaperidotite from Itaguara (São Francisco Craton, Brazil): Oldest Blueschist-Facies Fragment of Oceanic Moho?

Alexandre de Oliveira Chaves

Institute of Geosciences (IGC), Federal University of Minas Gerais (UFMG), Av. Antônio Carlos, 6627-Pampulha, Belo Horizonte, MG, CEP 31270-901, Brazil

Abstract: In close association with Paleoproterozoic retroeclogite and accretionary prism-related mica-quartz schist, a 2.13 Ga (metamorphic titanite U-Pb age) lawsonite/barroisite-bearing E-MORB signature metagabbro associated with spinel metaperidotite is found in the Itaguara Sequence from southern São Francisco craton, Brazil. Petrography and pressure-temperature equilibrium phase diagrams suggest that the metagabbro experienced blueschist-facies metamorphism, attaining peak metamorphic conditions at ~16 kbar and ~450 °C during subduction. The retrograde metamorphic path crossed epidote amphibolite-facies, in which the mineral assemblage found in metaperidotite (olivine, clinopyroxene, spinel, serpentine, chlorite, talc, and tremolite) was stable during a ca. 2.1 Ga continental collision-related exhumation that occurred between the Archean Campo Belo/Bonfim and Divinópolis complexes. This geological framework suggests that the metagabbro and adjacent spinel metaperidotite represent a subducted and exhumed blueschist-facies fragment of a Paleoproterozoic oceanic Mohorovičić (Moho) discontinuity, thus establishing the Itaguara metagabbro as the oldest-known occurrence of retrogressed blueschist and providing evidence for the activity of the modern-style plate tectonics more than 2 Gyr ago.

Keywords: Metagabbro and metaperidotite; Blueschist; Paleoproterozoic; Moho; São Francisco craton

1. Introduction

In many orogenic belts, rocks that have undergone subduction and exhumation processes can be found in their internal sectors, such as suture zones. To under-

*Corresponding Author:
Alexandre de Oliveira Chaves,
Institute of Geosciences (IGC), Federal University of Minas Gerais (UFMG), Av. Antônio Carlos, 6627-Pampulha, Belo Horizonte, MG, CEP 31270-901, Brazil;
Email: alochaves@yahoo.com.br

Received: 30 March 2024; **Received in revised form:** 16 May 2024; **Accepted:** 23 May 2024; **Published:** 14 June 2024

Citation: de Oliveira Chaves, A., 2024. 2.13 Ga Lawsonite/Barroisite-Bearing E-Morb Signature Metagabbro Associated with Spinel Metaperidotite from Itaguara (São Francisco Craton, Brazil): Oldest Blueschist-Facies Fragment of Oceanic Moho? *Earth and Planetary Science*. 3(2): 14–40. DOI: https://doi.org/10.36956/eps.v3i2.1068

DOI: https://doi.org/10.36956/eps.v3i2.1068

stand the geotectonic timeline of these belts, it is necessary to estimate the pressure (*P*) and temperature (*T*) paths of high-pressure subduction-related rocks [1]. Blueschists are rocks that form due to subduction, indicating high-pressure burial at relatively low temperatures (low *T/P* rocks) [2,3]. The oldest blueschists known so far are Neoproterozoic, some of which are found alongside strongly serpentinized plagioclase- or spinel peridotite [1]. Despite this, it is believed that subduction of oceanic crust to mantle depths has been occurring since 3 billion years ago [4]. So, a major question is: Where are the pre-0.8 Ga blueschists?

An investigation into the Itaguara Sequence (IS) of the southern São Francisco Craton (SFC) has revealed that a Paleoproterozoic accretionary prism was formed above a paleo-subduction zone. The study showed that during a continental collision at around 2.05 ± 0.05 Ga, the metamorphic peak achieved ~18.5 kbar and ~626 °C [5,6]. This episode of syn-collisional metamorphism has also been regionally described between 2.10 and 2.05 Ga from titanite and monazite geochronology [7,8]. The study also found that a 2.20 ± 0.05 Ga retroeclogite with E-MORB signature occurs in IS included in suture zone formed by a collision between the Archean Campo Belo/Bonfim and Divinópolis Complexes, close to the cited accretionary wedge [9]. Similar amphibole eclogite facies metamorphic peak stage of 17–20 kbar and 600–700 °C have been described for these retroeclogites during the same ca. 2.1 Ga continental collision [9].

Several studies demonstrate that barroisite-bearing metabasites retrometamorphosed at epidote amphibolite-facies have been formed in association with tectonic processes of subduction followed by collision-related exhumation [10,11]. By using petrography, mineral chemistry, thermobarometry, geochemistry, and titanite U-Pb geochronology, the petrology of the recently discovered lawsonite and barroisite-bearing metagabbro associated with spinel metaperidotite, which occur alongside 2.16 Ga amphibolites (zircon U-Pb age [12]) from the Paleoproterozoic IS, is herein presented.

Lawsonite is a diagnostic mineral of paleo-subduction zone processes [13,14]. Given that the oldest known occurrences of lawsonite-bearing blueschists are from Neoproterozoic era [1,14], the presence of lawsonite in these Paleoproterozoic rocks from IS may represent a new constraint in the age of blueschists on Earth. The possibility of this rock association to represent the subduction and exhumation of blueschist-facies fragment of Paleoproterozoic oceanic Mohorovičić discontinuity (Moho—boundary between oceanic crust and mantle) is also herein evaluated.

2. Geological Setting

The São Francisco craton (SFC), located in Brazil, is part of a paleoplate that was consolidated at the end of the Paleoproterozoic era. It is the South American equivalent of the African Congo Craton [15]. The southern region of SFC is surrounded by Neoproterozoic orogenic belts, such as the Araçuaí Belt [16] in the East and the Brasília Belt [17] in the West (Figure 1A). The Archean core of the southern SFC, which dates back to 3.2–2.6 billion years ago, comprises mainly of granite-gneisses terranes [18] and greenstone belts (Figure 1B, 1C). The Rio das Velhas Supergroup is a part of this region and includes a mix of mafic to ultramafic rocks, intermediate to felsic volcanic with volcanoclastic rocks and clastic sediments [19,20]. The Minas Supergroup is relatively younger and is composed of clastic and chemical metasedimentary units, which includes the Quadrilátero Ferrífero mining district (Figure 1B) that contains banded iron formations with a minimum deposition age of ~2.0 Ga [21].

Machado Filho et al. [22] characterized the Divinópolis Metamorphic Complex, which is part of the Archean granite-gneiss basement. Another study in this basement by Teixeira et al. [18] identified three complexes—Campo Belo, Bonfim, and Belo Horizonte (Figure 1B, 1C)—each consisting of various types of rocks, including gneisses, migmatites, granitoids, and felsic, mafic and ultramafic rocks. The Archean core of the southern SFC has undergone four periods of magmatism [23–25]. The first event, known as Santa Barbara, dates back to 3.22–3.20 Ga, and is associated with the formation of the Paleoarchean Tonalite-Trondhjemite-Granodiorite (TTG) crust. The second event, Rio das Velhas I, occurred between 2.92–2.85 Ga, and contributed to the growth of the crust. The third event, Rio das Velhas II, took place during the Neoarchean period (2.80–2.76 Ga) and was followed by a period of convergence and voluminous potassic magmatism. This period is believed to have stabilized the southern part of the SFC between 2.75–2.68 Ga [24], and was called the Mamona event [25]. A study on the zircon provenance of the sedimentary record preserved in the Rio das Velhas Supergroup suggests the presence of a succession of magmatic arcs and convergent basins in the region until ~2.7 Ga [26].

During the Rhyacian-Orosirian cycle, which took place around 2.2–1.9 Ga, a significant period of crustal growth took place in several parts of the SFC and adjacent crustal blocks of South America. This event was previously known as "Transamazonian" [18] and has now been renamed Minas accretionary orogeny in the southern SFC [28]. This period is associated with the accretion of juvenile crust that formed the Mineiro Belt [29,30] and led to extensive reworking of terranes located at the margins of the craton [31]. According to Alkmim and Marshak [32], a significant part of the southern portion of the São Francisco paleoplate was in the foreland of the Transamazonian orogeny. The NW limit between these Paleoproterozoic terrains and the Archean core is defined by the NE-SW Jeceaba Bom-Sucesso lineament (JBSL in Figure 1B), as suggested by several studies [28,30,33].

Most Paleoproterozoic rocks are located to the southeast of the JBSL, but there are a few exceptions. One of these exceptions is the Kinawa migmatite of the Itapecerica Metamorphic Complex, where 2.7 billion-year-old TTG metagranodiorites from the Campo Belo Metamorphic Complex were partially melted during the Paleoproterozoic in the Cláudio Shear Zone (CSZ in Figure 1B). U-Pb SHRIMP zircon age of 2.05–2.03 Ga [34] confirm the existence of a Paleoproterozoic episode previously documented from monazite in sillimanite-cordierite-garnet-biotite gneiss (graphite-rich khondalite) near CSZ [35]. Additionally, several generations of mafic dyke swarms (Figure 1B) are recognized in the southern SFC [36].

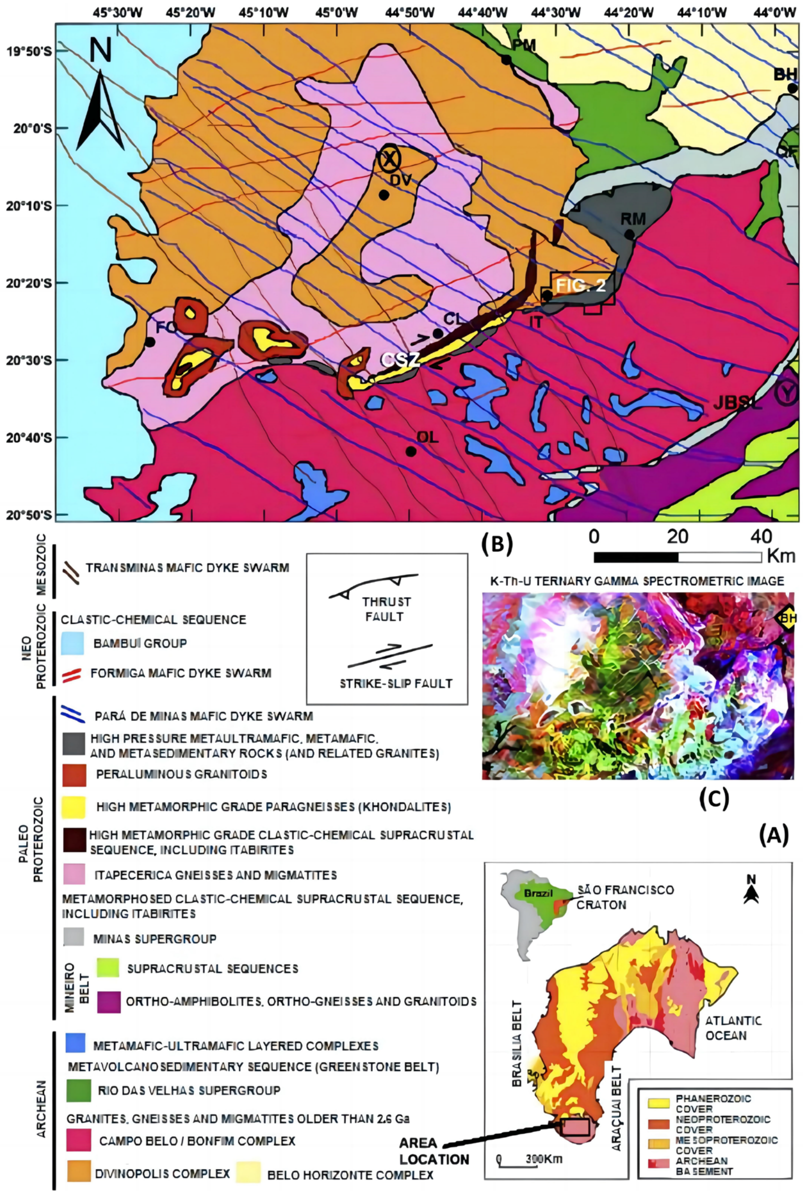

Figure 1. Regional geological setting. (**A**) The São Francisco Craton. (**B**) Geological map of the Southern São Francisco Craton [5], permitted reproduction—copyright Elsevier. QF—Quadrilátero Ferrífero, JBSL—Jeceaba-Bom Sucesso lineament, CSZ—Cláudio shear zone. Cities: BH—Belo Horizonte, PM—Pará de Minas, DV—Divinópolis, RM—Rio Manso, IT—Itaguara, FO—Formiga, CL—Cláudio, OL—Oliveira. (**C**) K-Th-U ternary gamma spectrometric image of the Southern São Francisco Craton [27].

The region between Itaguara and Crucilândia towns hosts a narrow NE-SW belt where the Itaguara Sequence (IS) is located. This sequence comprises metamorphosed mafic-ultramafic layered rocks (Figure 2), including amphibolites (zircon U-Pb age of 2.16 Ga [12]) and talc-actinolite metaultramafites (talc nephrites). The metaultramafic rocks are strongly folded and deformed and contain coarse olivine nodules within a fine to medium grained groundmass of talc and actinolite. Additionally, the IS also features metasedimentary rocks such as iron formations, quartzites, mica-quartz schists, and the Córrego do Peixoto granite (crystallization U-Pb age of ~2.0 Ga [12]). The region is intersected by high angle dextral strike-slip and northwestward reverse faults, as well as two mafic dyke systems [37].

Chaves and Porcher's research [9] shows that Itaguara region, where IS is located, contains retrogressed eclogite (retroeclogite). This type of rock formed during the Paleoproterozoic era, when the Archean Divinópolis and Campo Belo/Bonfim Complexes collided to create a suture zone. The retroeclogite in Itaguara has garnet porphyroblasts embedded in a fine-grained matrix of amphibole, biotite, and quartz, with scarce omphacite and phengite. The rock's protolith was E-MORB (T_{DM} ~2.47 Ga), which underwent eclogitization around 2.20 ± 0.05 Ga (garnet and whole rock Sm-Nd isochronic age), as evidenced by omphacite formation during high-pressure prograde stage at a depth of around 70 km. During the continental collision around 2.1 Ga, the rock experienced an amphibole eclogite-facies metamorphic peak stage of 17–20 kbar and 600–700 °C. Tectonic exhumation-related decompression during collision likely led to partial melting of the eclogitic rock. Finally, during the orogenic collapse, a late-stage decompression estimated between 5–8 kbar and 550–650 °C under amphibolite-facies overprint caused the appearance of kelyphitic reaction rims (symplectite) around garnet crystals [9].

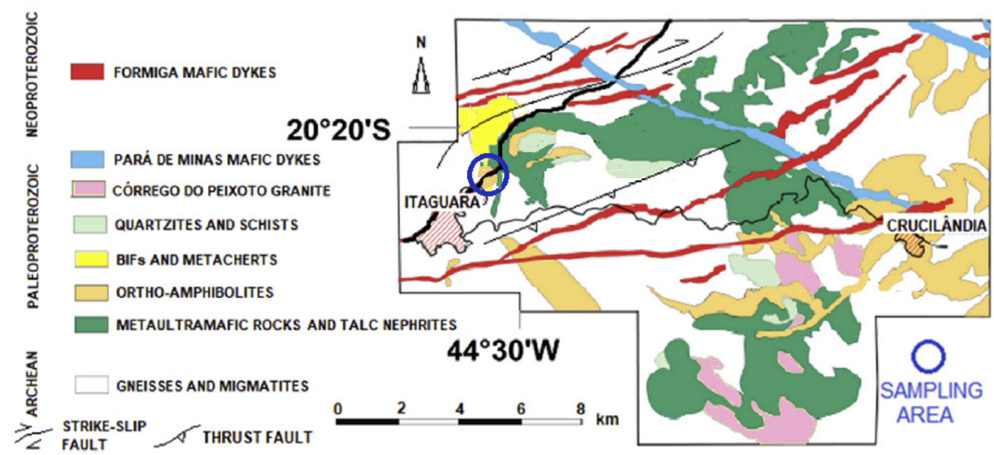

Figure 2. Geological map of the Itaguara Sequence (IS), with metagabbro sampling location close to the Itaguara town (modified from Goulart and Carneiro [37] and Chaves et al. [5], permitted reproduction—copyright Elsevier).

Studies conducted on the mica-quartz schist and Córrego do Peixoto granite from IS have revealed that they underwent metamorphic peak at around 2.05 ± 0.05 Ga. The metamorphism led to amphibole eclogite-facies at a depth of approximately 60 km, with a geothermal gradient of about 10 °C/km, which is typical of subduction zones in continental collision settings [5,6]. The high-pressure (*HP*) mica-quartz schist underwent a decompression process triggered by continental collision-related tectonic exhumation, leading to partial melting and generation of the peraluminous (S-type) syn-collisional Córrego do Peixoto granite. The granite solidus field was in wet conditions, and the metamorphism occurred at around 18.5 kbar and 626 °C. The monazite age of 1.93 ± 0.02 Ga found in both the mica-quartz schist and granite is probably related to the late-stage orogenic collapse-related decompression, with amphibolite-facies overprint [5,6].

The IS extends northeast towards the Rio Manso Sequence (RMS) near the town of Rio Manso. RMS consists of a variety of meta-ultramafic rocks such as spinel-bearing ultramafic rocks, metabasalts and other types. The spinel-bearing ultramafic rocks were categorized into four petrographic types including orthopyroxene and olivine-bearing rocks, Ca amphibole-bearing rocks, talc and/or serpentine-rich rocks, and talc-bearing rocks [38]. In the region, a type of olivine can be found exhibiting a pseudo-spinifex texture that was formed during high-grade metamorphism alongside talc and serpentine. According to the analysis conducted by Pinheiro and Nilson [38], this olivine texture is similar to the spinifex texture found in metakomatiitic rocks in the RMS. Additionally, there are other rocks in the area, such as iron formations, garnet amphibolites, and metasedimentary rocks like quartzites and sericite-quartz schists. These rocks have been interpreted as Archean in age [38] but IS and RMS have been estimated as Paleoproterozoic in the legend of Figure 1 due to the geochronological results [5] and differences in K-Th-U gamma spectrometric signal between them and Rio das Velhas Supergroup rocks (Figure 1C).

According to a study by Chaves et al. [5], the mica-quartz schist found in the IS region is believed to be a component of a Paleoproterozoic accretionary wedge formed above a paleo-subduction zone. Ophiolites, which are typically associated with an accretionary wedge in continental collision settings, are represented in the IS and RMS by metamafic-ultramafic rocks. Additionally, the NW boundary between the Archean core and Paleoproterozoic terrains in the IS and RMS region can now be demarcated by this ophiolitic landscape and is limited southwestward by the Cláudio shear zone (CSZ).

3. Methods

After field work close to Itaguara town (Figure 2), polished thin sections of distinct bands of metagabbro and associated metaperidotite (Figure 3) from Paleoproterozoic IS suture zone (coordinates 20.367986 S and 44.470016 W) were prepared for petrographic investigation and mineral microanalyses. After examining the metagabbro minerals with a petrographic optical microscope, they were further analyzed at the Federal University of Minas Gerais (UFMG) using a JEOL electron microprobe (EMP). The analysis was performed using a wavelength dispersive X-ray spectroscopy (WDS) under operating conditions of 15 kV accelerating voltage and 20 nA sample current. Calibration was done using oxide and silicate standards including quartz (Si), rutile (Ti), corundum (Al), almandine (Fe), periclase (Mg), rhodonite (Mn), anorthite (Ca), jadeite (Na), and sanidine (K). The counting times were 20 seconds on the peak and 10 seconds on the background. Three spectrometers were used simultaneously and the ZAF correction procedure was applied. To prevent interaction between different crystals during analyses, the electron beam was focused on the minimum size of 2 micrometers. Garnet compositional maps were generated through WDS.

Figure 3. Field exposure of metagabbro and metaperidotite. (**A**) Bluish metagabbro top view and highlight of the sample 2 (brownish, under the hammer) taken from foliation surface. (**B**) Bluish layered metagabbro side view and highlighted positions of the samples 1 (light-colored) and 3 (dark-colored) in the rock. (**C**) Dark-colored metaperidotite with highlighted position of the sample 4. (**D**) Layered metaperidotite side view.

Rock samples 1 and 2, which displayed different mineralogical associations, were sent to the SGS-Geosol Laboratory in Brazil for whole rock geochemical analysis. The samples were milled in a tungsten mill and then melted with lithium metaborate and dilute nitric digestion. The laboratory conducted ICP-OES (Inductively Coupled Plasma-Optical Emission Spectrometry) analysis to determine the major elements and five trace elements (Ba, Nb, Sr, Y, Zr). In addition, they used ICP-MS (Inductively Coupled Plasma Mass Spectrometry) to analyze fourteen rare earth elements and other trace elements. The detection limit is approximately 0.01% for the major elements and 1 ppm for the other elements. The accuracy of the analysis ranges from 1–2% for the relative standard deviation. The laboratory also determined the loss of ignition (LOI) through mass difference after heating the samples at 1000 °C.

The 2020 version of the Theriak-Domino software [39] with ds62 database [40] was utilized to produce *P–T* equilibrium phase diagrams (*P–T* pseudosections) using bulk rock compositions in the system Na-Ca-K-Fe-Mg-Al-Si-H-Ti-O (NCKFMASHTO). All fluid phases were considered as H_2O. Presented throughout the text, conventional geothermobarometers have also been used in order to investigate *P* and *T* during the metamorphic evolution of the metagabbro.

Ten crystals of metamorphic titanite were selected from sample 1 to constraint the age of metamorphism of the metagabbro, since this mineral was not found in a few igneous preserved areas of the rock, but only in the metamorphosed ones, which show idiomorphic titanite. U-Pb geochronology was used on 30 to 50 micrometres polished thin section, and the data were obtained using a Thermo Scientific Element II single collector (SF) ICP-MS coupled to a CETAC UV Nd: YAG-213 nm laser ablation system of the Isotopic Geochemistry Laboratory at Federal University of Ouro Preto—UFOP—Brazil. The acquisition method produced over 810 mass scans during 25 seconds of background acquisition and 30 seconds of sample ablation. Each analysis utilized a spot size of 40 µm with a repetition rate of 10 Hz and a laser fluence of approximately 3.5 J/cm^2. The depth penetration was 0.6 µm/s, and the integration time was 0.9 seconds. Raw counts were adjusted offline for background signal, instrumental mass bias, and time-dependent elemental fractionation. The data were reduced by Glitter software [41,42] and an in-house spreadsheet [43,44]. Due to the varying initial Pb ratios of the titanite and the technical difficulties in measuring ^{204}Pb via LA-ICP-MS [45], none of the U-Pb analyses from UFOP were corrected for Pb_c. The ages have been reported accordingly as lower intercepts on the Tera-Wasserburg Concordia diagram, obtained from Isoplot package [46]. All uncertainties on dates/ages are reported as 2s. Four titanite reference material known as Bear Lake, BLR-1, Khan River and Mount Painter have been dated to check measurements, and produced their expected ages of 1064 Ma, 1054 Ma, 542 Ma and 444 Ma respectively [47].

4. Results

4.1 Field Exposure, Petrography, Mineral Chemistry and Metamorphic Assemblages

In field exposure (Figure 3), there are only scattered blocks of bluish metagabbro and dark-colored metaperidotite alongside the road and it was not possible to find geological contact between them. Results of petrographic investigation and mineral microanalyses in different bands of layered metagabbro (samples 1, 2 and 3) and associated metaperidotite (sample 4), shown in Figure 3, are presented below with suggestions of the respective probable prograde, peak and retrograde metamorphic phase assemblages. This paper employs the mineral name abbreviations provided by Whitney and Evans [48].

Sample 1

Remains of igneous texture containing labradoritic plagioclase (An_{51-55}) and augitic clinopyroxene ($Wo_{48}En_{34}Fs_{18}$) have been found in sample 1 of the metagabbro (Figure 4A) and representative analyses of these minerals are presented in Table 1. Figure 4B shows plagioclase (Pl), clinopyroxene (Cpx) and magnetite (Mag) scattered in a granoblastic texture. The metamorphism advanced and new minerals like garnet (Grt), clinozoisite (Czo), titanite (Ttn) and quartz (Qz) appeared (Figure 4C, 4D and Table 2), which represent the prograde metamorphic phase assemblage.

Lawsonite (Lws—preserved inside garnet that was altered to chlorite is highlighted in grey circle of Figure 4D) is probably the mineral formed during a metamorphic peak. During retrograde metamorphism, phengite (Ph) was formed, garnet (Grt) was replaced by chlorite (Chl—Figure 4D) and Cpx was replaced by magnesium-hornblende (Hbl) as shown in Figure 4E and Table 2. Subhedral to euhedral prehnite (Prh) crystals are also found in sample 1 of the metagabbro (Figure 4F and Table 2) and they seem to represent the final evolution of the rock. Thus, Ph, Chl, Hbl and, finally, Prh should be the retrograde metamorphic mineral assemblage.

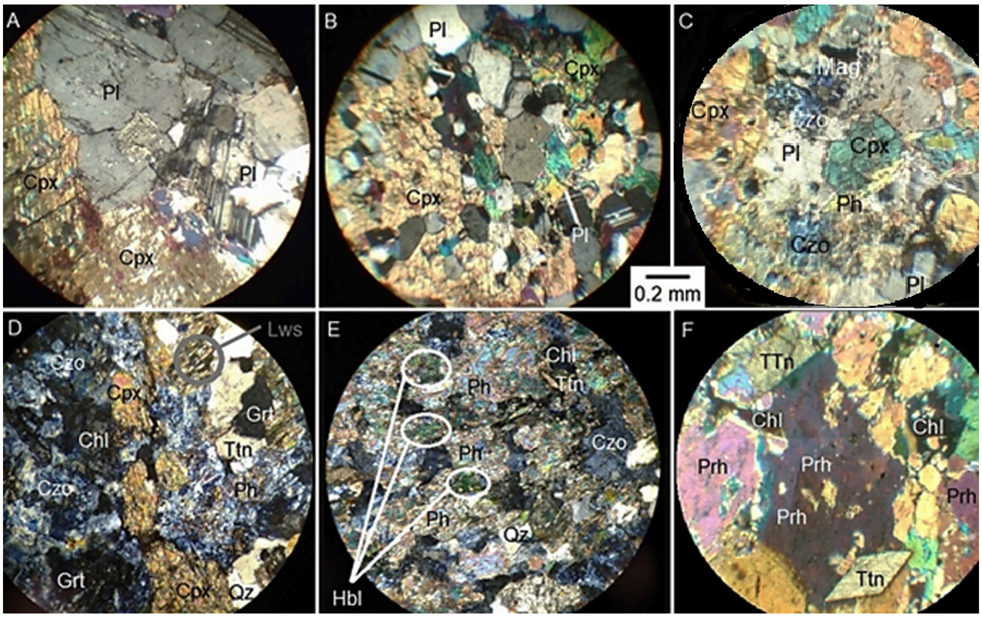

Figure 4. Photomicrographs of sample 1 under crossed polarizers. (**A**) Preserved igneous gabbroic texture. (**B**) Metagabbro with recrystallized plagioclase (Pl) and clinopyroxene (Cpx). (**C**) Magnetite (Mag), phengite (Ph) and clinozoisite (Czo). (**D**) Clinopyroxene (Cpx), garnet-Grt (in substitution to chlorite-Chl), quartz (Qz), clinozoisite (Czo), titanite (Ttn) and lawsonite (Lws—preserved inside garnet). (**E**) Hornblende (Hbl), clinozoisite (Czo), and more phengite (Ph). (**F**) Prehnite (Prh) and titanite (Ttn).

Table 1. Representative analyses of plagioclase (Pl) and clinopyroxene (Cpx) from a preserved igneous portion of the metagabbro (sample 1).

	Pl-1	**Pl-2**	**Pl-3**	**Pl-4**		**Cpx-1**	**Cpx-2**
SiO_2	55.24	54.92	55.32	54.75	SiO_2	54.03	53.17
TiO_2	0.03	0.05	0.00	0.07	TiO_2	0.04	0.00
Al_2O_3	27.53	27.87	27.72	27.75	Al_2O_3	0.76	0.72
FeO	0.09	0.17	0.13	0.14	FeO	10.77	10.90
MnO	0.01	0.00	0.02	0.00	MnO	0.54	0.50
MgO	0.08	0.10	0.04	0.06	MgO	11.40	11.76
CaO	11.00	11.52	11.10	11.25	CaO	22.78	23.05
Na_2O	5.47	5.32	5.74	5.80	Na_2O	0.31	0.31
K_2O	0.11	0.07	0.14	0.06	K_2O	0.12	0.10
Total	99.56	100.01	100.19	99.89	Total	100.75	100.50
32 ox					6 ox		
Si	10.02	9.94	9.99	9.93	Si	2.02	2.00
Ti	0.00	0.01	0.00	0.01	Al	0.05	0.03
Al	5.88	5.94	5.90	5.93	Fe	0.34	0.34
Fe	0.01	0.03	0.02	0.02	Mn	0.02	0.02
Ca	2.14	2.23	2.15	2.18	Mg	0.63	0.66
Na	1.92	1.86	2.01	2.04	Ca	0.91	0.93
K	0.02	0.02	0.03	0.01	Na	0.02	0.02
Total	20.01	20.03	20.09	20.13	K	0.01	0.00
					Total	3.98	4.00
An	52.32	54.27	51.27	51.55	Wo	47.93	47.72
Ab	47.08	45.33	47.98	48.13	En	33.39	33.87
Or	0.61	0.40	0.75	0.32	Fs	18.68	18.42

Table 2. Representative analyses of clinozoisite (Czo), phengite (Ph), lawsonite (Lws), chlorite (Chl), titanite (Ttn), hornblende (Hbl) and prehnite (Prh) from metamorphosed portion of the metagabbro (sample 1).

	Czo-1	**Czo-2**		**Ph-1**	**Ph-2**	**Ph-3**	**Ph-4**	**Ph-5**	**Ph-6**	**Ph-7**
SiO_2	39.68	39.62	SiO_2	49.68	49.26	49.48	49.89	49.43	49.52	49.59
TiO_2	0.05	0.00	TiO_2	0.02	0.06	0.00	0.00	0.13	0.01	0.00
Al_2O_3	29.27	29.10	Al_2O_3	32.81	32.37	33.47	32.40	32.64	32.82	32.75
Fe_2O_3	4.29	4.61	FeO	1.96	1.60	1.81	1.84	1.58	1.68	1.54
MnO	0.16	0.00	MnO	0.00	0.04	0.00	0.04	0.02	0.00	0.03
MgO	0.13	0.24	MgO	2.86	2.56	2.26	2.47	2.53	2.66	2.45
CaO	23.88	23.91	CaO	0.17	0.24	0.15	0.17	0.17	0.20	0.17
Na_2O	0.17	0.16	Na_2O	0.18	0.30	0.13	0.22	0.16	0.21	0.14
K_2O	0.08	0.04	K_2O	10.03	10.31	10.16	10.90	10.82	10.66	10.03
Total	97.72	97.67	Total	97.71	96.73	97.46	97.93	97.47	97.75	96.71
25 ox			11 ox							
Si	6.24	6.25	Si	3.21	3.22	3.21	3.24	3.22	3.21	3.23
Ti	0.01	0.00	Al(IV)	0.79	0.78	0.79	0.76	0.78	0.79	0.77
Al	5.43	5.41	Al(VI)	1.71	1.72	1.76	1.71	1.72	1.72	1.75
Fe(iii)	0.25	0.27	Fe(ii)	0.11	0.09	0.10	0.10	0.09	0.09	0.08
Mn	0.02	0.00	Mn	0.00	0.00	0.00	0.00	0.00	0.00	0.00
Mg	0.03	0.06	Mg	0.28	0.25	0.22	0.24	0.25	0.26	0.24
Ca	4.02	4.04	Ca	0.01	0.02	0.01	0.01	0.01	0.01	0.01
Na	0.05	0.05	Na	0.02	0.04	0.02	0.03	0.02	0.03	0.02
K	0.02	0.01	K	0.83	0.86	0.84	0.90	0.90	0.88	0.83
Total	16.07	16.08	Total	6.96	6.98	6.94	6.99	6.99	6.99	6.94

Table 2 (continued)

	Lws-1	**Lws-2**		**Chl-1**	**Chl-2**		**Ttn-1**		**Hbl-1**	**Hbl-2**		**Prh-1**	**Prh-2**
SiO_2	38.99	38.68	SiO_2	28.16	28.60	SiO_2	31.62	SiO_2	46.16	46.52	SiO_2	44.80	44.23
TiO_2	0.00	0.03	TiO_2	0.30	0.39	TiO_2	37.82	TiO_2	0.56	0.71	TiO_2	0.04	0.00
Al_2O_3	32.52	32.71	Al_2O_3	18.56	18.48	Al_2O_3	1.36	Al_2O_3	8.35	9.07	Al_2O_3	24.06	24.44
FeO	0.86	0.28	FeO	27.66	27.22	FeO	0.51	FeO	13.16	13.28	FeO	0.21	0.16
MnO	0.02	0.03	MnO	0.24	0.28	MnO	0.16	MnO	0.41	0.30	MnO	0.12	0.18
MgO	0.21	0.10	MgO	12.64	12.76	MgO	0.04	MgO	13.58	13.30	MgO	0.11	0.10
CaO	17.28	17.94	CaO	0.12	0.19	CaO	28.48	CaO	11.71	11.47	CaO	26.56	26.76
Na_2O	0.77	0.90	Na_2O	0.02	0.02	Na_2O	0.06	Na_2O	1.05	1.10	Na_2O	0.10	0.15
K_2O	0.16	0.08	K_2O	0.65	0.71	K_2O	0.03	K_2O	0.20	0.25	K_2O	0.03	0.02
Total	90.79	90.75	Total	88.35	88.65	Total	100.08	Total	95.18	96.00	Total	96.02	96.05
								23 ox					
								Si	6.88	6.89			
			28 ox					Al(IV)	1.12	1.11			
8 ox			Si	5.96	6.01	5 ox		Al(VI)	0.35	0.48	11 ox		
Si	2.00	1.99	Al(IV)	2.04	1.99	Si	1.03	Fe(iii)	0.30	0.11	Si	3.06	3.02
Ti	0.00	0.00	Al(VI)	2.59	2.59	Ti	0.93	Ti	0.06	0.08	Ti	0.00	0.00
Al	1.97	1.98	Ti	0.05	0.06	Al	0.05	Fe(ii)	1.34	1.54	Al	1.94	1.97
Fe	0.04	0.01	Fe(ii)	4.89	4.79	Fe	0.01	Mn	0.05	0.04	Fe	0.01	0.01
Mn	0.00	0.00	Mn	0.04	0.05	Mn	0.00	Mg	3.02	2.94	Mn	0.01	0.01
Mg	0.02	0.01	Mg	3.99	4.00	Mg	0.00	Ca	1.87	1.82	Mg	0.01	0.01
Ca	0.95	0.99	Ca	0.03	0.04	Ca	0.99	Na	0.30	0.32	Ca	1.94	1.96
Na	0.08	0.09	Na	0.01	0.01	Na	0.00	K	0.04	0.05	Na	0.01	0.02
K	0.01	0.00	K	0.18	0.19	K	0.00	Total	15.34	15.36	K	0.00	0.00
Total	5.06	5.07	Total	19.77	19.73	Total	3.02	Name	Mg-Hbl	Mg-Hbl	Total	6.98	7.00

Source: Amphibole name according to Leake et al. [49].

Sample 2

Visible in hand sample and with pleochroism in shades of blue, elongated barroisite (Brs) crystals occur partially replaced by brownish tschermakite (Ts) amphibole (Figure 5A and Table 3). Biotite (Bt) and phengite (Ph) also occur associated with these minerals (Figure 5A). With irregular edges, few almandine garnet porphyroblasts appear, being replaced by chlorite (Figure 5B and 5C), which is the most abundant mineral of sample 2, responsible by lepidoblastic texture. Table 4 shows the chemical composition of 12 spots from one edge to the other in garnet. Core-rim chemical zoning can be seen in Figure 6, where EMP Fe (richer in rim) and Mg (richer in core) concentration maps (Figure 6A and 6B) are presented with a quantitative graphical profile from spot X to spot X' (Figure 6C).

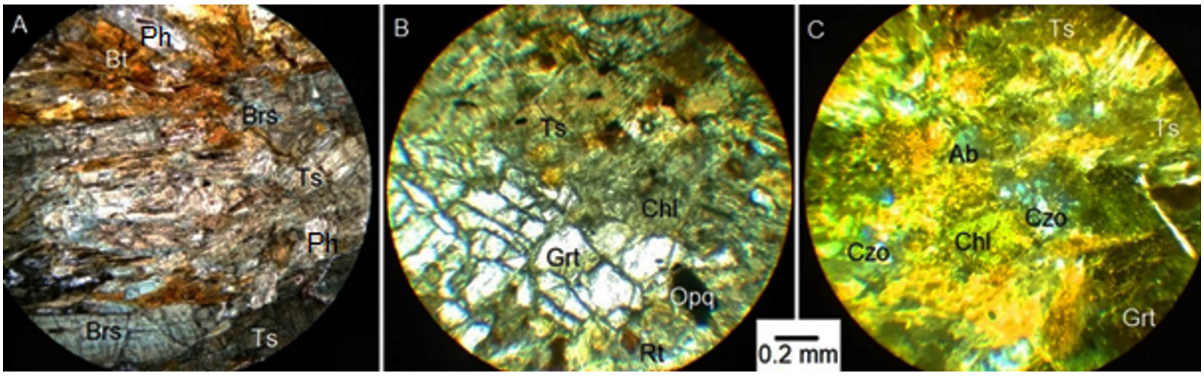

Figure 5. Photomicrographs of sample 2 under uncrossed polarizers. (**A**) Bluish barroisite (Brs) is being replaced by tschermakite (Ts) and biotite (Bt). Some phengite (Ph) also appears. (**B**) Garnet (Grt) replacement by chlorite (Chl). Opq—opaque mineral, Rt—Rutile. (**C**) Photomicrography of sample 2 under crossed polarizers, showing tschermakite (Ts), clinozoisite (Czo), albite (Ab), garnet (Grt) and chlorite (Chl).

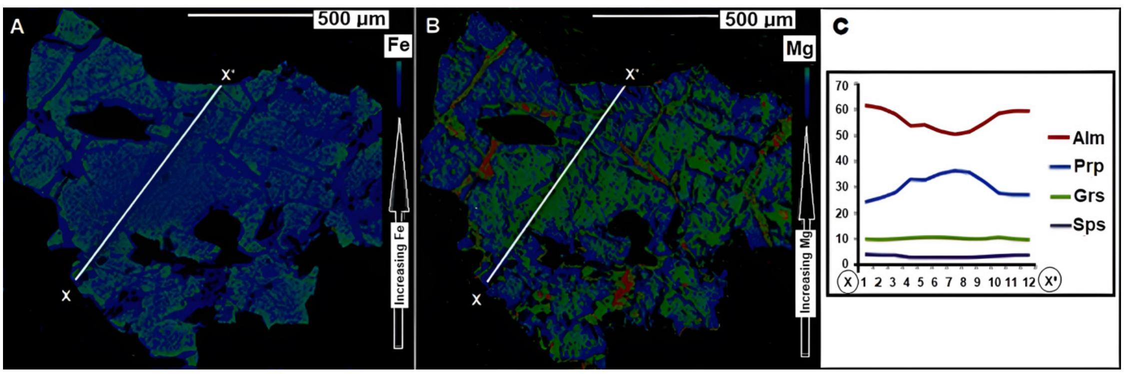

Figure 6. EMP-WDS garnet compositional maps. (**A**) Fe, (**B**) Mg, (**C**) Quantitative graphical profile from spot X to spot X' (data from Table 4). Prp = pyrope. Alm = almandine, Grs = grossular. Sps = spessartine.

Table 3. Representative analyses of tschermakite (Ts), barroisite (Brs), plagioclase (Pl), clinozoisite (Czo) and chlorite (Chl) from sample 2.

	Ts-1	Ts-2	Ts-3	Ts-4		Brs-1	Brs-2		Pl-5		Czo-3		Chl-3
SiO_2	43.31	43.04	43.57	43.08	SiO_2	49.69	49.72	SiO_2	71.03	SiO_2	39.86	SiO_2	29.01
TiO_2	0.71	0.39	0.83	0.53	TiO_2	0.72	0.74	TiO_2	0.00	TiO_2	0.04	TiO_2	0.02
Al_2O_3	16.04	16.06	16.20	15.78	Al_2O_3	13.10	13.08	Al_2O_3	18.80	Al_2O_3	29.82	Al_2O_3	22.05
FeO	11.75	12.14	11.25	11.36	FeO	11.36	11.37	FeO	0.44	Fe_2O_3	4.06	FeO	17.18
MnO	0.22	0.30	0.27	0.39	MnO	0.27	0.26	MnO	0.03	MnO	0.10	MnO	0.34
MgO	12.96	12.71	12.57	12.89	MgO	10.68	10.84	MgO	0.12	MgO	0.05	MgO	19.92
CaO	10.83	11.10	10.56	11.31	CaO	9.59	9.63	CaO	0.70	CaO	23.35	CaO	0.13
Na_2O	2.43	2.50	2.38	2.42	Na_2O	1.96	1.90	Na_2O	8.77	Na_2O	0.09	Na_2O	0.04

Table 3 continued

	Ts-1	Ts-2	Ts-3	Ts-4		Brs-1	Brs-2		Pl-5		Czo-3		Chl-3
K_2O	0.22	0.19	0.31	0.19	K_2O	0.29	0.32	K_2O	0.19	K_2O	0.05	K_2O	0.05
Total	98.46	98.44	97.95	97.94	Total	97.65	97.86	Total	100.08	Total	97.40	Total	88.75
23 ox					23 ox								
Si	6.25	6.23	6.29	6.25	Si	7.07	7.06	32 ox					
Al(IV)	1.75	1.77	1.71	1.75	Al(IV)	0.93	0.94	Si	12.28			28 ox	
Al(VI)	0.97	0.97	1.05	0.95	Al(VI)	1.27	1.25	Ti	0.00	25 ox		Si	5.74
Fe(iii)	0.00	0.00	0.00	0.00	Fe(iii)	0.00	0.03	Al	3.83	Si	6.26	Al(IV)	2.26
Ti	0.08	0.04	0.09	0.06	Ti	0.08	0.08	Fe(ii)	0.06	Ti	0.00	Al(VI)	2.88
Fe(ii)	1.42	1.47	1.36	1.38	Fe(ii)	1.35	1.32	Ca	0.13	Al	5.52	Ti	0.00
Mn	0.03	0.04	0.03	0.05	Mn	0.03	0.03	Na	2.94	Fe(iii)	0.24	Fe(ii)	2.84
Mg	2.79	2.74	2.71	2.79	Mg	2.27	2.29	K	0.04	Mn	0.01	Mn	0.06
Ca	1.67	1.72	1.63	1.76	Ca	1.46	1.47	Total	19.29	Mg	0.01	Mg	5.87
Na	0.68	0.70	0.67	0.68	Na	0.54	0.52			Ca	3.93	Ca	0.03
K	0.04	0.04	0.06	0.04	K	0.05	0.06	An	4.18	Na	0.03	Na	0.02
Total	15.67	15.72	15.60	15.70	Total	15.05	15.04	Ab	94.51	K	0.01	K	0.01
Name	Ts	Ts	Ts	Ts	Name	Brs	Brs	Or	1.32	Total	16.00	Total	19.71

Source: Amphibole names according to Leake et al. [49].

Table 4. Chemical analyses of 12 spots from one edge to the other in garnet crystal from sample 2, as shown in Figure 6.

	Grt1	Grt2	Grt3	Grt4	Grt5	Grt6	Grt7	Grt8	Grt9	Grt10	Grt11	Grt12
	rim	rim	rim	core	core	core	core	core	core	rim	rim	rim
SiO_2	38.37	38.50	38.41	38.80	39.42	39.02	39.43	40.63	38.80	38.93	38.80	38.52
TiO_2	0.03	0.09	0.04	0.15	0.12	0.03	0.04	0.05	0.07	0.01	0.01	0.01
Al_2O_3	21.51	22.26	21.45	22.72	22.43	22.49	22.23	21.31	22.25	22.29	22.40	22.56
FeO	27.72	27.68	26.68	24.27	23.99	23.64	23.50	23.78	24.98	26.72	26.79	26.30
MnO	1.75	1.64	1.71	1.23	1.22	1.25	1.29	1.28	1.32	1.52	1.57	1.61
MgO	6.17	6.58	7.17	8.39	8.13	9.03	9.54	9.27	8.27	7.10	6.85	6.72
CaO	3.46	3.47	3.60	3.62	3.67	3.78	3.79	3.63	3.60	3.71	3.55	3.34
Na_2O	0.13	0.06	0.11	0.06	0.14	0.10	0.06	0.00	0.13	0.09	0.09	0.10
K_2O	0.03	0.04	0.03	0.03	0.02	0.08	0.02	0.03	0.06	0.02	0.07	0.08
Total	99.18	100.32	99.19	99.26	99.14	99.41	99.89	99.99	99.48	100.40	100.12	99.24
24 ox												
Si	6.04	5.98	6.02	5.98	6.07	6.00	6.02	6.18	6.00	6.01	6.01	6.01
Ti	0.00	0.01	0.00	0.02	0.01	0.00	0.01	0.01	0.01	0.00	0.00	0.00
Al	3.99	4.07	3.96	4.13	4.07	4.07	4.00	3.82	4.05	4.05	4.09	4.15
Fe	3.65	3.59	3.50	3.13	3.09	3.04	3.00	3.03	3.23	3.45	3.47	3.43
Mn	0.23	0.22	0.23	0.16	0.16	0.16	0.17	0.17	0.17	0.20	0.21	0.21
Mg	1.45	1.52	1.67	1.93	1.87	2.07	2.17	2.10	1.91	1.63	1.58	1.56
Ca	0.58	0.58	0.61	0.60	0.61	0.62	0.62	0.59	0.60	0.61	0.59	0.56
Total	15.96	15.97	15.99	15.94	15.88	15.96	15.98	15.90	15.97	15.96	15.95	15.92
Prp	24.48	25.77	27.89	33.14	32.62	35.11	36.45	35.72	32.27	27.71	27.06	27.11
Alm	61.72	60.81	58.24	53.81	54.01	51.57	50.36	51.43	54.69	58.51	59.35	59.54
Grs	9.86	9.77	10.08	10.27	10.58	10.57	10.39	10.05	10.10	10.41	10.08	9.67
Sps	3.94	3.66	3.79	2.77	2.79	2.75	2.79	2.81	2.94	3.37	3.52	3.68

In sample 2 from metagabbro are still found accessory rutile (Rt—analyzed with TiO_2 = 99.13 and FeO = 0.43 by WDS-EMP), opaque minerals (Opq), albite (Ab_{95}) and clinozoisite (Figure 5B, 5C and Table 3). Brs, Almandine Grt, Rt and Czo are prograde metamorphic minerals and Ph would be probably of the metamorphic peak. Ts, Bt, Chl, and Ab seem to be retrograde minerals. Qz is almost nonexistent.

Sample 3

With granonematoblastic texture, sample 3 has mineralogy composed of magnesium hornblende (Hbl), clinozoisite (Czo) and andesine plagioclase ($Ab_{54–63}$), with respective analyses presented in Table 5. Some portions of the rock are constituted by Hbl and Czo, and metagabbro was renamed to epidote hornblendite (Figure 7A). Other ones are constituted by Hbl and plagioclase (Pl), with sporadic Czo (Figure 7B). This assemblage suggests that sample 3 passed through epidote amphibolite metamorphic facies.

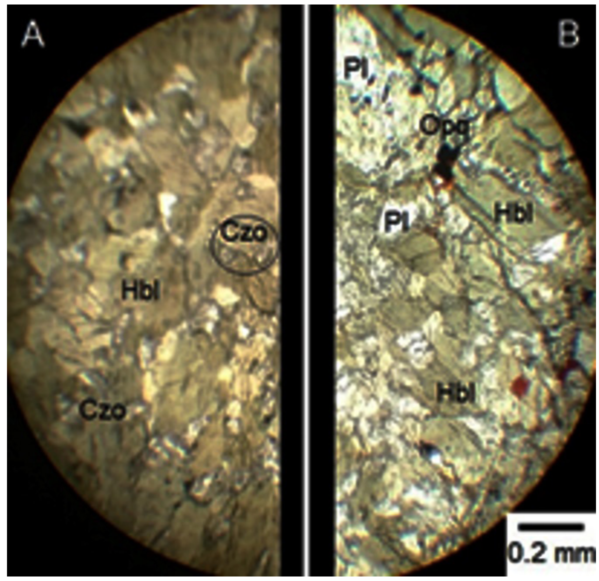

Figure 7. Photomicrographs of sample 3 under uncrossed polarizers. (**A**) Clinozoisite (Czo) and hornblende (Hbl). (**B**) Plagioclase (Pl) and hornblende (Hbl).

Table 5. Representative analyses of plagioclase (Pl), clinozoisite and hornblende from sample 3.

	Pl-6	**Pl-7**	**Pl-8**		**Czo-4**		**Hbl-3**	**Hbl-4**
SiO_2	57.65	58.26	58.71	SiO_2	38.39	SiO_2	46.97	47.09
TiO_2	0.36	0.00	0.05	TiO_2	0.06	TiO_2	0.86	0.80
Al_2O_3	26.05	26.72	25.59	Al_2O_3	29.74	Al_2O_3	13.51	13.37
FeO	0.20	0.14	1.83	Fe_2O_3	2.89	FeO	12.10	12.27
MnO	0.07	0.00	0.01	MnO	0.26	MnO	0.31	0.28
MgO	0.06	0.13	0.51	MgO	0.10	MgO	11.00	11.01
CaO	8.75	7.57	6.02	CaO	25.26	CaO	11.04	11.08
Na_2O	6.20	5.64	6.57	Na_2O	0.27	Na_2O	2.21	2.18
K_2O	0.18	0.83	0.73	K_2O	0.26	K_2O	0.24	0.18
Total	99.51	99.28	100.02	Total	97.21	Total	98.24	98.24
32 ox						23 ox		
Si	10.39	10.48	10.58			Si	6.75	6.77
Ti	0.05	0.00	0.01			Al(IV)	1.25	1.23
Al	5.53	5.66	5.44	25 ox		Al(VI)	1.04	1.03
Fe(ii)	0.03	0.02	0.28	Si	6.06	Fe(iii)	0.00	0.00
Ca	1.69	1.46	1.16	Ti	0.01	Ti	0.09	0.09
Na	2.17	1.97	2.30	Al	5.53	Fe(ii)	1.45	1.47
K	0.04	0.19	0.17	Fe(iii)	0.17	Mn	0.04	0.03
Total	19.90	19.77	19.92	Mn	0.03	Mg	2.36	2.36
				Mg	0.02	Ca	1.70	1.71
				Ca	4.27	Na	0.61	0.61
An	43.35	40.37	32.06	Na	0.08	K	0.04	0.03
Ab	55.62	54.38	63.34	K	0.05	Total	15.34	15.33
Or	1.03	5.26	4.61	Total	16.23	Name	Mg-Hbl	Mg-Hbl

Source: Amphibole name according to Leake et al. [49].

Sample 4

Metaperidotite has spinel wehrlite as protolith and shows its original mineralogy of olivine (Ol), clinopyroxene (Cpx) and spinel (Spl) is replaced by serpentine (Srp), chlorite (Chl), talc (Tlc) and tremolite (Tr), as shown in Figure 8A, 8B, 8C and 8D. According to Winter [50], in metaperidotites the mineral association Ol-Cpx-Srp-Tlc-Tr is stable around 500 °C and between 6 and 12 kbar.

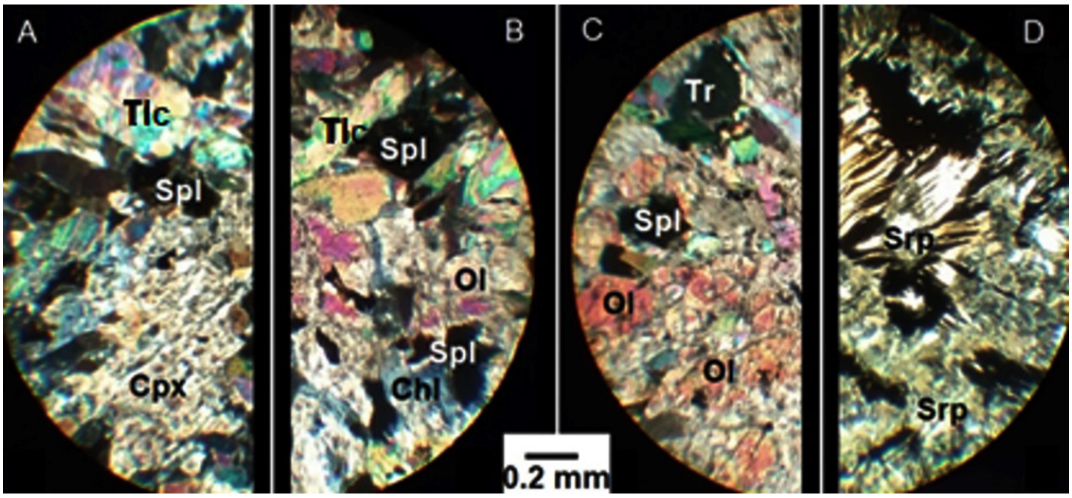

Figure 8. Photomicrographs of sample 4 under crossed polarizers. Olivine (Ol), clinopyroxene (Cpx), spinel (Spl), serpentine (Srp), chlorite (Chl), talc (Tlc) and tremolite (Tr) represent the rock mineralogy. (**A**), (**B**), (**C**) and (**D**) are different parts of the same thin section.

4.2 Thermobarometry

P–*T* pseudosections have been obtained for samples 1 (High Si and Ca) and 2 (Low Si and Ca) of the metagabbro and are respectively shown in Figures 9 and 10. Usually described in low *T/P* subduction-related rocks, sodic-calcic amphiboles (like Brs—found in sample 2, Figure 5A) appeared in both pseudosections. Typical of blueschist-facies metamorphism, lawsonite (Lws) found in sample 1 (Figure 4D) appeared only in pseudosection of sample 1 (Figure 9) above 14 kbar (low Ca does not favor the appearance of Lws in sample 2). Rutile (Rt) found in sample 2 (Figure 5B) appeared in pseudosection of sample 2 (Figure 10) above 8 kbar. Based on these observations from petrography and pseudosections, it is reasonable to suggest that metagabbro attained high-pressure conditions (> 10 kbar).

The prograde *P*–*T* path herein proposed in both pseudosections followed toward metamorphic peak conditions determined by the occurrence of Lws in Figure 9 and by the presence of Ph in Figure 10, inside blueschist metamorphic facies. Therefore, it is herein suggested that the prograde path had a trajectory around 25 °C/kbar (~250 °C/GPa) in both pseudosections, which in turn pointed together to metamorphic peak around 16 kbar and 450 °C, corresponding to ~50 km depth subduction (Figures 9 and 10).

Chlorite (Chl) is the most abundant mineral in sample 2 (Figure 5B and 5C) and appeared in all stability fields of equilibrium assemblages in pseudosection of Figure 10. However, in sample 1 pseudosection (Fiure 9), the first appearance of Chl, described in petrography as replacing garnet (Figure 4D), was around 16 kbar and 500 °C, condition that drives the retrograde section of the *P*–*T* path to this region of *P* and *T*, from blueschist-facies to epidote amphibolite-facies. Albite (Ab) has been described in petrography as a retrograde mineral in sample 2 (Figure 5C) and its first appearance in Figure 10 took place around 4 kbar during final retrograde section of the proposed *P*–*T* path.

Taken together, tschermakite replacing barroisite crystals (sample 2—Figure 5A) and garnet rim (sample 2—Figure 6) seem to indicate metagabbro exhumation (drop in *P* and *T*) occurred after metamorphic peak. Regarding conventional thermometry, the pressure-independent Grt–Hbl Fe–Mg geothermometer [51] has been tentatively used to estimate *T* during metagabbro exhumation (retrograde metamorphism). Average tschermakite compositions (Table 3) and average compositions of the garnet rim (Table 4) yielded 521 ± 26 °C. This temperature is consistent with epidote amphibolite-facies and agrees with an intermediate section of the retrograde path in pseudosection of Figure 10.

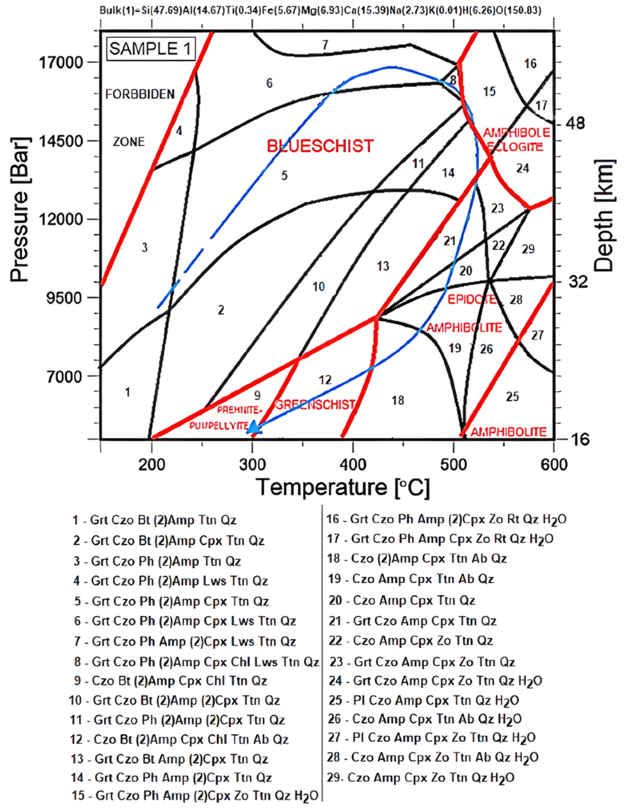

Figure 9. *P*–*T* pseudosection of sample 1 showing stability fields of several equilibrium mineral assemblages and the probable metamorphic evolution (path in blue) of the metagabbro from Itaguara Sequence. Mineral abbreviations are as in text and metamorphic facies are separated by red lines. Forbidden metamorphic zone and approximate depths are after Palin et al. [52].

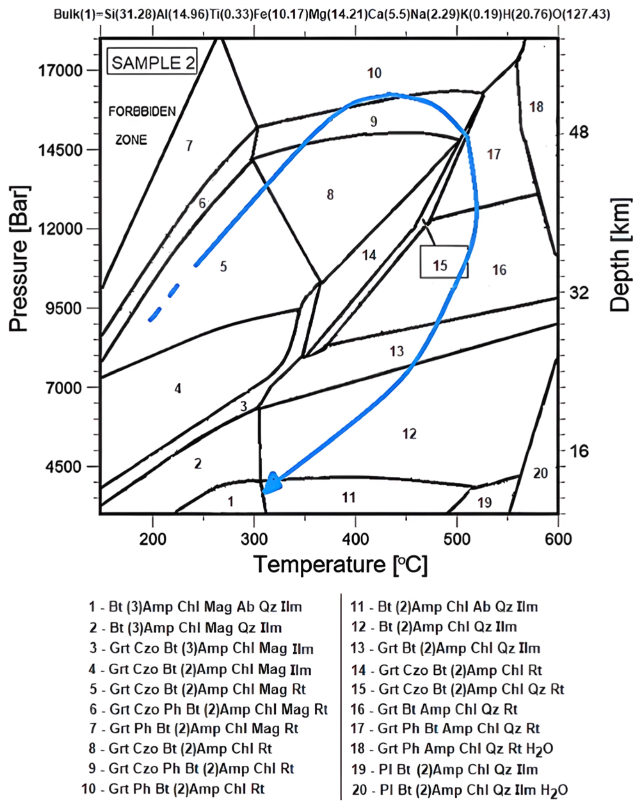

Figure 10. *P*–*T* pseudosection of sample 2 showing stability fields of several equilibrium mineral assemblages and the probable metamorphic evolution (path in blue) of the metagabbro from Itaguara Sequence. Mineral abbreviations are as in text. Forbidden metamorphic zone and approximate depths are after Palin et al. [52].

Phengite from sample 1 is low-Si (Table 2) and therefore understood herein as a retrograde metamorphic mineral. For phengite with Si < 3.25 apfu, Kamzolkin et al. [53] have proposed the following equation to calculate *P*:

$P(\mathrm{GPa}) = [0.023T(^{\circ}\mathrm{C}) + 5.99\mathrm{Si} + 1.76\mathrm{Al} + 12.89(\mathrm{Mg} + \mathrm{Fe}) - 31.91]/10$

By using average apfu data from phengite analyses (Si < 3.25 apfu; Table 2) and by considering $T = 521$ °C previously obtained, the pressure found for metagabbro using this equation is 0.81 ± 0.34 GPa (8.1 ± 3.4 kbar). This pressure occurs in epidote amphibolite-facies and also seems to represent metagabbro exhumation, in agreement with intermediate section of the retrograde path in pseudosection of Figure 9. In this figure, the retrograde path ends around 300 °C in which prehnite (Prh) found in rock (Figure 4F) is stable. The mineral assemblage constituted by magnesium hornblende (Hbl), clinozoisite (Czo) and andesine plagioclase (Ab_{54-63}) from sample 3 is additional evidence for metagabbro path through epidote amphibolite-facies. The mineral assemblage Ol-Cpx-Srp-Tr found in metaperidotite (sample 4—Figure 8) is stable around 500 °C and between 6 and 12 kbar [48], which are the respective *T* and *P* of the retrograde path.

4.3 Geochemistry

Geochemical data of samples 1 (high silica and Ca and low Mg and Fe) and 2 (low silica and Ca and high Mg and Fe) are presented in Table 6. When plotted in SiO_2 versus Nb/Y diagram (Figure 11A) of Xia and Li [54], both metagabbro samples are classified as sub-alkaline basalt.

Table 6. Chemical composition of samples 1 and 2. Major elements oxides in % and trace elements in ppm. LOI—Lost On Ignition.

	Sample 1	Sample 2
SiO_2	52.82	41.01
TiO_2	0.50	0.58
Al_2O_3	13.79	16.64
Cr_2O_3	0.10	0.14
FeOt	7.51	15.94
MnO	0.30	0.35
MgO	5.15	12.50
CaO	15.91	6.73
Na_2O	1.56	1.55
K_2O	0.01	0.20
P_2O_5	0.10	0.08
LOI	1.04	4.08
Total	98.79	99.80
Co	41.60	91.80
Ni	212.00	352.00
Cs	0.71	1.70
Rb	2.90	12.20
Ba	47.00	105.00
Sr	144.00	47.00
Nb	3.53	3.90
Ta	1.46	1.00
Y	12.93	30.49
Zr	43.00	68.00
Hf	1.21	1.52
V	124.00	268.00
Cu	40.00	42.00
Ga	10.00	19.00
Th	2.80	1.60
U	0.72	0.44
La	6.20	8.60
Ce	11.70	13.10
Pr	1.26	2.05
Nd	6.80	9.50
Sm	1.80	2.50
Eu	0.53	0.60
Gd	2.07	3.10
Tb	0.31	0.45
Dy	2.34	3.41
Ho	0.43	0.71
Tm	0.23	0.28
Er	1.70	2.36
Yb	1.70	2.00
Lu	0.24	0.29

In AFM ternary diagram (Figure 11B) after Irvine and Baragar [55] and in Zr-Ti/100-Y×3 ternary diagram (Figure 11C) of Pearce and Cann [56], the metagabbro protolith is classified as MORB-like tholeiitic basalt. Both chondrite-normalized rare earth element variation plot (Figure 11D) and primitive mantle-normalized trace element variation plot (Figure 11E) (normalization and reference curves after Sun and McDonough [57]) reveal that metagabbro has an E-MORB pattern. Negative anomalies of Nb and Ti can be related to fluid release from protolith during dehydration under subduction process [58,59]. E-MORB signature of the metagabbro protolith is reinforced in TiO_2/Yb versus Nb/Yb diagram [60] and Y/Nb versus Zr/Nb diagram [54], respectively shown in Figures 11F and 11G.

4.4 U-Pb Geochronology

Figure 12A shows the laser spots on the metamorphic titanite crystals of the metagabbro from sample 1. The acquired U-Pb data of 56 spots are presented in Table 7. The lower intercept on the Tera-Wasserburg Concordia diagram (Figure 12B) yielded an age of 2135 ± 15 Ma for the metamorphic titanite crystals.

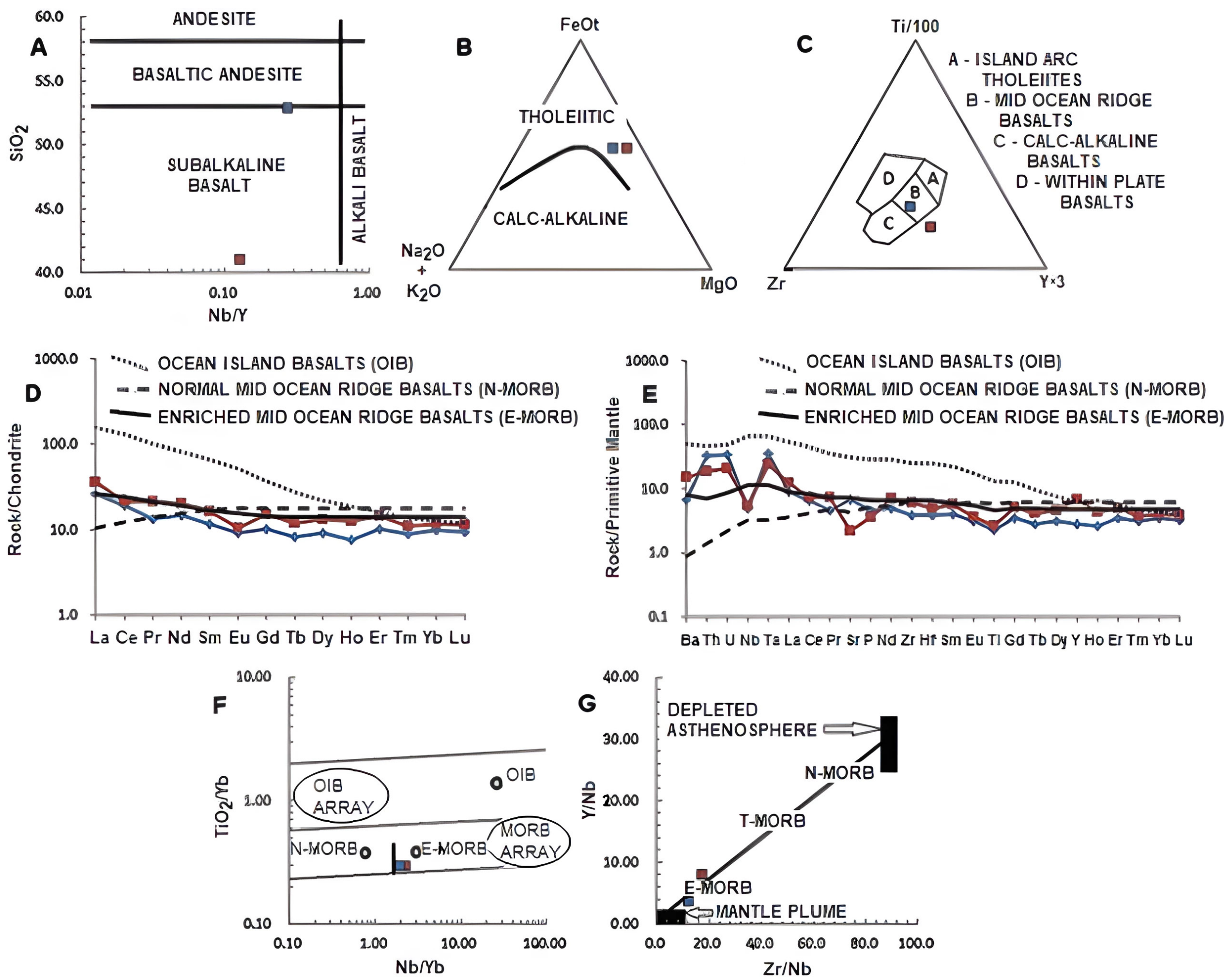

Figure 11. Geochemical diagrams. (**A**) SiO_2 versus Nb/Y classification diagram [54]. (**B**) AFM ternary diagram after Irvine and Baragar [55]. (**C**) Zr-Ti/100-Y×3 ternary diagram [56]. (**D**) Chondrite-normalized rare earth element variation plot (normalization and reference curves after Sun and McDonough [57]. (**E**) Trace element variation plot normalized to primitive mantle (normalization and reference curves after Sun and McDonough [57]). (**F**) TiO_2/Yb versus Nb/Yb diagram [60]. (**G**) Y/Nb versus Zr/Nb diagram [54], where T-MORB is transitional MORB. Blue square—sample 1, red square—sample 2.

Figure 12. Titanite U-Pb geochronology. (**A**) Photomicrographs under reflected light of the laser spots on titanite crystals. (**B**) $^{207}Pb/^{206}Pb$ versus $^{238}U/^{206}Pb$ Tera-Wasserburg Concordia diagram of the titanite crystals from metagabbro of sample 1.

Table 7. U-Pb data of titanite crystals from metagabbro of the sample 1.

SPOT	238U (ppm)	232Th (ppm)	238U/ 232Th	207Pb (cps)	206Pb (cps)	208Pb (cps)	202Hg (cps)	204Pb (cps)	207Pb/ 206Pb	2sigma (%)	207Pb/ 235U	2sigma (%)	206Pb/ 238U	2sigma (%)	Rho
073	20.42597	49.887464	2.4423542	14430.48	94483.62	6.16603E	10149.22	315.1973	0.16462	2.991611	9.47583	6.366376	0.41747	5.619698	0.88271
GRN	357	09	86	379	148	-06	752	904	1357	22	8779	271	4748	312	539
074	22.02747	50.910894	2.3112453	13359.75	100095.5	8.75198E	9878.707	238.9732	0.14406	1.553306	8.14340	5.479352	0.40997	5.254573	0.95897
GRN	255	26	85	755	615	-06	737	871	0064	228	0217	839	8328	94	7108
075	23.84391	59.761717	2.5063715	14077.49	107617.5	4.34539E	9717.630	247.0460	0.14119	3.393505	7.94470	6.395832	0.40808	5.421327	0.84763
GRN	785	57	6	718	058	-06	355	357	6461	667	6253	161	6999	173	4371
076	21.63064	42.190555	1.9504988	13199.92	95160.65	4.13025E	9449.427	261.5403	0.14973	1.573270	8.21032	5.700760	0.39768	5.479369	0.96116
GRN	873	38	46	745	919	-07	647	464	2542	342	3871	746	8303	81	4668
077	19.95918	42.833110	2.1460346	11806.47	89330.71	1.51305E	9279.520	234.3989	0.14266	3.710265	7.99775	7.348539	0.40659	6.343103	0.86317
GRN	908	38	01	598	293	-06	714	827	2619	175	6945	34	004	559	8826
078	21.54277	51.479238	2.3896290	16739.66	101588.4	1.8133E	9106.669	375.5749	0.17788	3.194491	10.5212	6.385263	0.42896	5.528726	0.86585
GRN	436	69	16	727	52	-06	471	395	7042	206	6005	518	5304	447	7209
079	33.74793	80.035284	2.3715607	24494.87	154288.8	5.93324E	8986.140	515.6280	0.17139	5.307225	9.84173	7.552999	0.41645	5.374118	0.71152
GRN	728	84	92	862	361	-06	645	731	6344	448	326	039	5652	767	1177
080	32.78370	80.351959	2.4509725	18966.11	144057.5	1.82625E	8842.803	235.8367	0.14205	1.393628	7.83948	5.423331	0.40025	5.241213	0.96641
GRN	507	75	06	251	126	-05	93	9	2575	443	8904	371	5552	879	9627
083	32.34701	79.220966	2.4490967	18411.78	143639.5	2.74176E	8520.398	264.4506	0.13838	5.115925	7.74924	7.451349	0.40612	5.417555	0.72705
GRN	419	07	11	633	553	-05	861	446	9519	851	8617	081	0695	336	6977
084	16.45603	36.765566	2.2341698	12510.71	75753.59	1.06471E	8327.622	337.3164	0.17833	3.473300	10.3657	6.712201	0.42157	5.743677	0.85570
GRN	044	62	23	128	543	-05	719	327	0147	868	018	17	2884	013	6923
085	24.31691	48.785879	2.0062529	16141.71	106378.7	2.21271E	8302.722	288.3736	0.16385	1.561659	9.04625	5.717352	0.40041	5.499940	0.96197
GRN	391	35	13	003	609	-06	706	649	3529	879	6696	98	6378	32	3196
086	26.68487	59.891758	2.2444083	16817.72	117140.2	1.4421E	8188.840	251.4843	0.15503	2.568988	8.62554	6.004815	0.40350	5.427532	0.90386
GRN	553	7	97	02	023	-05		034	7544	177	1948	541	4364	536	3324
087	27.12061	67.684255	2.4956752	17446.93	120009.1	7.89305E	8094.761	318.6304	0.15699	4.233375	8.79750	6.901828	0.40640	5.451033	0.78979
GRN	783	47	79	523	059	-06	08	143	817	432	7646	221	944	41	5578
088	30.47530	73.109057	2.3989608	18430.53	133750.8	1.53849E	8089.213	279.5207	0.14881	2.611352	8.29715	5.865665	0.40437	5.252320	0.89543
GRN	222	87	81	335	565	-05	004	928	4161	696	7719	389	4545	206	4679
089	30.85969	83.647459	2.7105732	17583.27	134539.9	6.73158E	8102.706	240.9285	0.14109	2.669311	7.80280	5.888256	0.40108	5.248460	0.89134
GRN	382	82	26	718	137	-06	274	569	6548	539	1963	068	1768	292	3758
090	39.27197	111.76637	2.8459579	22366.30	170581.7	9.24697E	8075.564	355.2544	0.14160	7.419853	7.83179	9.320661	0.40111	5.640966	0.60521
GRN	138	77	12	992	47	-07	84	213	8527	348	4853	23	659	411	0969
093	38.13008	107.93210	2.8306285	26395.93	168466.9	1.62367E	8219.148	533.1675	0.16923	5.266283	9.55101	7.615440	0.40932	5.501016	0.72235
GRN	374	34	45	241	254	-05	464	593	1933	654	576	236	2833	857	0473
094	41.10446	116.22869	2.8276413	24965.81	173769.2	1.06963E	8356.830	386.1904	0.15515	6.683281	8.38546	8.944927	0.39197	5.945206	0.66464
GRN	725	3	92	508	478	-05	255	702	4028	788	0343	73	8801	19	5525
095	29.52214	70.829164	2.3991875	20213.74	129390.2	8.90451E	8534.823	441.3089	0.16874	12.82390	9.45662	16.12380	0.40645	9.773671	0.60616
GRN	622	51	11	37	597	-06	928	935	2138	443	1602	768	3802	232	3967

Table 7 (continued)

SPOT	238U (ppm)	232Th (ppm)	238U/ 232Th	207Pb (cps)	206Pb (cps)	208Pb (cps)	202Hg (cps)	204Pb (cps)	207Pb/ 206Pb	2sigma (%)	207Pb/ 235U	2sigma (%)	206Pb/ 238U	2sigma (%)	Rho
096	31.24811	66.251663	2.1201808	18679.47	135016.2	6.00308E	8683.953	361.7018	0.14943	4.436075	8.26282	6.919592	0.40101	5.310554	0.76746
GRN	812	14	98	057	756	-06	111	471	9389	303	5564	14	6486	707	6434
097	32.41054	63.386682	1.9557423	17370.04	133566.4	1.21155E	8909.600	251.0024	0.14033	3.139365	7.40845	6.238531	0.38286	5.391072	0.86415
GRN	839	5	63	892	473	-05	228	895	9056	852	9603	715	7138	25	7224
098	30.52436	87.022787	2.8509286	19358.95	132776.9	5.29092E	9173.551	260.5522	0.15749	4.222857	8.76176	6.872553	0.40348	5.422127	0.78895
GRN	461	01	97	248	682	-06	203	123	269	502	9495	167	7557	032	3814
099	25.59008	57.997037	2.2663874	13968.49	105521.3	1.10531E	9267.892	225.7773	0.14299	1.445565	7.55941	5.731875	0.38341	5.546596	0.96767
GRN	016	21	78	587	848	-05	559	385	368	502	6228	244	592	631	5742
100	24.94615	79.411356	3.1833106	15492.46	109030.4	9.75757E	9514.036	275.3492	0.15349	8.743278	8.61874	10.55116	0.40724	5.906107	0.55975
GRN	337	75	92	817	249	-06	785	553	2212	697	8448	267	5773	965	8972
103	27.47258	70.764989	2.5758402	15422.69	115854.7	3.08223E	9853.669	244.0629	0.14346	1.410316	7.79394	5.517737	0.39400	5.334457	0.96678
GRN	461	24	52	372	632	-06	936	75	7769	691	0568	984	4761	732	3444
104	24.59990	74.143974	3.0139938	18083.53	109566.0	3.56831E	9877.010	388.8998	0.17772	5.895736	10.2069	11.18747	0.41652	9.507887	0.84986
GRN	885	22	59	735	644	-08	058	955	7888	942	1536	667	1726	26	879
105	22.62568	57.942769	2.5609288	15052.73	99482.13	2.92293E	9977.973	274.8256	0.16263	7.674436	9.27862	9.709666	0.41378	5.948163	0.61260
GRN	507	86	59	57	47	-06	567	672	3236	352	7858	481	351	57	2254
106	29.61442	103.53201	3.495999	18479.25	129611.8	1.21988E	10034.65	326.7687	0.15371	6.130314	8.70503	8.436849	0.41073	5.796522	0.68704
GRN	817	81	23	515	161	-05	13	912	1174	414	0221	368	6756	445	8232
107	30.66514	100.85839	3.2890241	19708.59	132171.7	8.63712E	9967.927	340.2836	0.16100	3.286110	8.95226	6.187112	0.40327	5.242312	0.84729
GRN	235	43	69	81	09	-06	149	351	1058	388	6132	716	6561	684	5487
108	37.17848	134.18170	3.6091223	21699.80	158188.8	8.77233E	9940.068	256.4643	0.14818	3.193279	8.15726	6.127185	0.39923	5.229280	0.85345
GRN	676	58	05	176	617	-07	119	372	9269	039	1317	447	2919	111	5499
109	43.30302	78.927347	1.8226752	28058.16	190390.9	1.09965E	9887.572	424.1339	0.15898	5.856060	9.06152	8.001359	0.41338	5.452367	0.68143
GRN	162	21	84	439	766	-07	629	195	2214	649	3338	785	1843	567	0121
110	28.48719	92.791993	3.2573233	15324.42	119332.9	4.10885E	9830.759	277.2527	0.13833	3.240841	7.52312	6.325911	0.39443	5.432688	0.85879
GRN	148	25	24	93	661	-06	841	62	3374	906	9248	923	0309	598	9279
113	30.39145	83.559177	2.7494301	17260.07	128740.1	5.23807E	9440.427	294.8785	0.14401	5.444437	7.96071	7.621771	0.40090	5.333808	0.69981
GRN	337	16	16	63	462	-06	025	076	7033	065	9212	772	103	207	2113
114	68.65429	155.99660	2.2722046	38715.83	286867.5	9.36235E	9317.825	378.3611	0.14578	2.574366	7.90088	5.795358	0.39306	5.192188	0.89592
GRN	191	37	84	343	597	-06	323	461	4707	879	2832	583	3195	005	1785
115	46.09509	70.744642	1.5347543	26363.89	192942.4	7.87243E	9251.833	293.1806	0.14747	0.973413	8.01471	5.423976	0.39414	5.335914	0.98376
GRN	046	08	82	963	01	-06	593	29	9241	606	8034	398	5054	722	437
116	49.19295	96.721396	1.9661637	30390.70	208279.2	1.71323E	9200.372	439.8430	0.15728	2.473910	8.67210	5.750388	0.39987	5.191024	0.90272
GRN	046	51	61	838	345	-05	053	365	9499	792	9846	47	4553	268	5841
117	63.12275	118.19245	1.8724221	34587.36	261430.8	8.94964E	9041.906	324.5115	0.14267	1.396762	7.68967	5.374993	0.390904	5.190338	0.96564
GRN	806	05	53	126	995	-06	337	566	1033	384	4223	583	672	222	5473
118	82.43484	245.80589	2.9818203	44713.56	344778.7	3.39377E	9131.865	343.5724	0.13994	1.102950	7.61430	5.293537	0.394626	5.177358	0.97805
GRN	618	98	25	933	904	-08	612	207	038	417	5786	206	267	065	2645

Table 7 (continued)

SPOT	238U (ppm)	232Th (ppm)	238U/ 232Th	207Pb (cps)	206Pb (cps)	208Pb (cps)	202Hg (cps)	204Pb (cps)	207Pb/ 206Pb	2sigma (%)	207Pb/ 235U	2sigma (%)	206Pb/ 238U	2sigma (%)	Rho
119	47.98642	117.83270	2.4555424	29370.53	201438.8	2.92243E	9087.702	399.6686	0.15732	1.739903	8.59795	5.504298	0.396377	5.222072	0.94872
GRN	664	88	73	616	188	-06	802	854	0426	22	0042	72	075	499	6216
120	61.11055	111.63183	1.8267193	35491.60	251500.4	1.96752E	9056.979	401.0685	0.15243	2.061977	8.16254	5.548418	0.388365	5.151038	0.92837
GRN	427	12	38	965	977	-05	316	36	4606	013	108	8	401	922	9617
143	33.15223	88.386302	2.6660739	21615.36	140445.5	4.68341E	8564.219	448.7637	0.16611	4.918362	9.13146	7.211002	0.398673	5.273354	0.73129
GRN	168	7	93	553	487	-06	033	712	9943	282	3968	554	493	748	2869
144	34.97304	125.53441	3.5894618	18757.13	142033.1	1.46756E	8351.006	198.2414	0.14253	1.359543	7.53124	5.544367	0.383215	5.375095	0.96946
GRN	672	8	8	427	53	-06	188	763	5183	425	0541	281	588	368	9571
145	31.41262	84.125499	2.6780790	20877.59	132860.5	5.39098E	8118.132	348.2995	0.16954	1.033028	9.31535	5.428977	0.398480	5.329788	0.98172
GRN	701	05	74	432	793	-07	614	981	7439	881	6377	405	4	644	9753
146	12.70807	35.080977	2.7605261	8321.056	57883.39	1.58953E	7979.221	193.7332	0.15514	3.446236	9.14104	19.17852	0.427336	18.86635	0.98372
GRN	671	84	31	14	398	-06	087	672	0148	851	1923	309	732	099	2829
147	25.74096	64.044767	2.4880481	17532.67	109561.6	1.12307E	7781.224	328.6821	0.17233	3.001863	9.53230	6.066393	0.401169	5.271617	0.86898
GRN	8	73	47	647	287	-05	047	129	3201	783	3445	981	243	376	6979
148	27.48189	85.396918	3.1073887	20400.54	119212.9	1.1314E	7620.668	443.7346	0.18435	4.282479	10.4116	6.781491	0.409607	5.258231	0.77537
GRN	13	59	04	604	095	-05	19	822	2752	822	2037	88	051	518	9756
149	20.18575	57.748270	2.8608423	11801.67	83008.01	3.17339E	7497.146	186.8148	0.15340	1.831142	8.15531	6.046171	0.385557	5.762213	0.95303
GRN	805	8	16	026	603	-05	767	27	8744	353	5406	221	692	473	5113
150	24.29375	56.826765	2.3391511	13869.25	100763.2	6.80112E	7374.845	188.6788	0.14850	2.160423	7.99080	5.894193	0.390245	5.483984	0.93040
GRN	486	62	91	243	326	-07	775	808	8745	685	9334	222	107	248	456
153	21.77676	61.495703	2.8239131	16905.46	97117.34	7.9012E	7061.172	457.0504	0.18778	10.70539	10.8406	12.95093	0.418699	7.288438	0.56277
GRN	861	62	67	616	446	-06	797	259	0653	223	4313	651	968	355	3074
154	31.07933	125.80126	4.0477466	17477.71	126722.0	4.06471E	6906.885	214.1057	0.14877	2.718415	7.84993	5.930564	0.382683	5.270845	0.88875
GRN	215	21	34	821	524	-06	937	066	3274	661	1292	894	432	877	9498
155	33.66996	142.19232	4.2231202	18544.72	138553.0	5.32289E	6810.173	206.7992	0.14429	1.450556	7.65793	5.647562	0.38491	5.458099	0.96645
GRN	901	96	98	086	106	-06	136	896	2455	617	5151	491	673	265	2213
156	28.91376	74.344355	2.5712444	14611.68	114015.4	1.48133E	6728.975	174.5013	0.13822	1.562627	7.03856	5.638861	0.369327	5.418021	0.96083
GRN	433	5	3	622	417	-06	505	959	0022	25	486	651	703	483	6037
157	20.67709	45.272041	2.1894780	12646.97	86100.55	6.29311E	6611.397	222.0937	0.15841	3.866557	8.54051	7.264789	0.391018	6.150357	0.84659
GRN	332	36	2	803	691	-06	493	46	0919	373	3142	016	744	187	8184
158	29.54467	75.149571	2.5435910	18656.53	123650.2	1.11462E	6568.141	361.5330	0.16270	8.115276	8.80006	10.20942	0.392260	6.194725	0.60676
GRN	587	68	01	453	969	-05	432	621	8228	039	4836	381	955	935	5479
159	25.71636	63.926992	2.4858482	14806.71	104372.5	3.21258E	6466.391	233.5183	0.15297	1.881229	7.97618	5.815922	0.378162	5.503264	0.94624
GRN	976	77	5	793	251	-05	606	346	3105	546	4808	044	839	905	1174
160	22.92704	54.299516	2.3683607	14204.64	93350.19	8.20983E	6477.874	210.7483	0.16406	4.079049	8.62529	6.730342	0.381282	5.353397	0.79541
GRN	645	06	12	697	609	-06	587	517	8733	922	67	742	563	534	232

5. Discussion and Conclusions

Preserved igneous texture in sample 1 has confirmed gabbro as the protolith of the investigated layered metabasic rock. Throughout the stability fields of the sodic-calcic amphibole (barroisite) crystals present in the metagabbro (Figures 9 and 10), the prograde path followed a ~25 °C/kbar subduction trajectory within the blueschist-facies field.

The reason why lawsonite is relatively scarce in the rock record worldwide can be explained by two factors. Firstly, it may be due to dehydration during subduction, which occurs before reaching the lawsonite stability field. As a result, the rock became H_2O undersaturated, which prevented the formation of lawsonite [61]. Alternatively, it could also be due to extensive retrogression during exhumation [62]. During this process, lawsonite often transforms into minerals like epidote. [13,14,61]. Remarkably, sample 1 preserves lawsonite because its formation occurred inside garnet, which has acted as a shieldin0g mineral that was slowly replaced by chlorite. Lawsonite is a remnant of metamorphic peak that probably occurred around 16 kbar and 450 °C in blueschist-facies as suggested by *P*–*T* path in Figure 9, and also sample 2 preserves rutile (stable Ti phase at higher *P*–*T* conditions; Figure 10) and phengite.

The estimated *P*–*T*–*t* paths for blueschists and eclogites containing lawsonite propose that temperature rise might occur before uplift, leading to the transformation of blueschist-facies assemblages into amphibolite-facies assemblages through recrystallization [62]. Hornblende, clinozoisite and andesine found in sample 3 register post-peak metamorphic conditions in epidote amphibolite-facies, during collision-related tectonic exhumation. This exhumation in turn also promoted the retrograde metamorphism of the metagabbro to prehnite/pumpellyite-facies conditions as indicated by prehnite found in sample 1 (Figure 9).

According to Maruyama et al. [1], orogenic peridotites are believed to be the uppermost mantle that constitutes the foundation of fragments of oceanic lithosphere added to the continental crust along subduction zones. These fragments are disintegrated parts of ophiolites—sections of oceanic crust and mantle that either separate from the descending slab and become part of the subduction zone's accretionary wedge, or get trapped between two terranes during an accretion event. In orogens, pieces of ultramafic bodies are situated along major fault zones that separate diverse terranes. These pieces are remnants of that once separated collisional terranes, and therefore mark the suture zone, which is the representation of the ancient subduction zone that happened before the collision [1]. The co-occurrence of blueschist-facies rocks with ultramafics, mafics, and sediments supports the hypothesis of a subduction-related origin [63]. Ophiolites can represent either a marginal sea behind an offshore island arc (like present-day Japan) in cases where the arc gets pushed back toward the continent behind it or typical oceanic crust between colliding continents. Spinel peridotites are smaller fragments of the presumed ophiolitic ultramafics [1].

Sample 4 was revealed to be spinel metawehrlite and the metamorphic assemblage with olivine, clinopyroxene, serpentine, chlorite, talc and tremolite is stable around 500 °C and between 6 and 12 kbar [50], the respective *T* and *P* of the exhumation-related retrograde metamorphism established for its associated metagabbro (Figures 9 and 10). Itaguara metagabbro E-MORB signature points out to oceanic setting and the association of the metagabbro to spinel metawehrlite between Campo Belo/Bonfim and Divinópolis Archean complexes suggests they represent subducted and exhumed meta-ophiolitic rocks. The accretionary prism (characterized by mica-quartz schist [5]) and retroeclogite [9] from Paleoproterozoic Itaguara Sequence (IS) supports the scenery of subduction and collision-related exhumation for the investigated region. The age of 2135 Ma found for titanite from metagabbro investigated herein (Figure 12), also belonging to this meta-ophiolitic sequence, seems to indicate the timing of the prograde blueschist-facies metamorphism of this rock, just before the ~2.1 Ga regional continental collision.

Evidence in support of the collision that occurred at about 2.1 Ga is found in monazite inclusions in corundum from IS [64]. Metamorphic corundum crystals are associated with continental collision zones and serve as tectonic indicators of continental collision. These crystals form due to metasomatism accompanying reactions between aluminosilicate-rich rocks (granitoids, gneisses, migmatite) and silica-poor ultramafic rocks [65]. The monazite found in metamorphic corundum between gneiss and metaultramafic rock from Itaguara revealed an age of 2126 ± 97 Ma, which is interpreted as the age of corundum growth. This supports the hypothesis of continental collision between Campo Belo/Bonfim and Divinópolis Archean complexes at that time [64], which was preceded by subduction of IS.

Brown and Johnson [66] and Palin et al. [52] suggest that the Paleoproterozoic Era may have experienced subduction-related processes similar to those seen on the Earth today. Just before tectonic exhumation related to the ca. 2.1 Ga collision between the Archean Campo Belo/Bonfim and Divinópolis complexes, the 2.13 Ga subduction setting envisaged for the IS is presented along X–Y section of the Figure 13 (this geodynamic illustration is the reconstruction previous to geological setting found along X–Y section of Figure 1B). Figure 13 shows the geological scenario of the accretionary prism (represented by mica-quartz schist [5]) and the 2.20 ± 0.05 Ga retroeclogite with an E-MORB signature [9] from the Paleoproterozoic IS close to the ~600 °C isotherm (~60 km depth).

The 2.13 Ga metagabbro and associated metaperidotite from Paleoproterozoic IS presented in Figure 3 occur alongside 2.16 Ga amphibolites (zircon U-Pb age [12]), as shown in Figure 2. Regarding the location of the investigated metagabbro and metaperidotite in Figure 13, they appear above ~500 °C isotherm (i.e., around 450 °C), corresponding to ~50 km depth attained during metamorphic peak. This is the location of the oceanic Moho discontinuity in the proposed subducting slab. Therefore, according to petrographic, chemical and thermobarometric data alongside geological setting presented in this manuscript, it is reasonable to suggest that lawsonite and barroisite-bearing metagabbro (although lawsonite and barroisite are not from the same sample, they are from the same rock) with E-MORB signature associated with spinel metaperidotite represent a subducted and exhumed Paleoproterozoic blueschist-facies meta-ophiolitic fragment of oceanic Moho, now exposed in IS of the southern São Francisco craton.

There are several Paleoproterozoic subducted and exhumed rocks represented by 2.10–1.80 Ga eclogite remnants [9,67–73] in collisional and accretionary orogens distributed in the new configuration of Columbia (Nuna) supercontinent, which has been elaborated by Chaves [74] and presented in Figure 14. The location of the subducted and exhumed Paleoproterozoic blueschist-facies metagabbro herein investigated is highlighted by white arrow in Figure 14. Based on all geological aspects presented in this manuscript, the IS metagabbro could be considered the oldest retrogressed blueschist known so far, constraining the age of such rocks to Paleoproterozoic, pushing back considerably the previous notion of Neoproterozoic as the oldest age of blueschists.

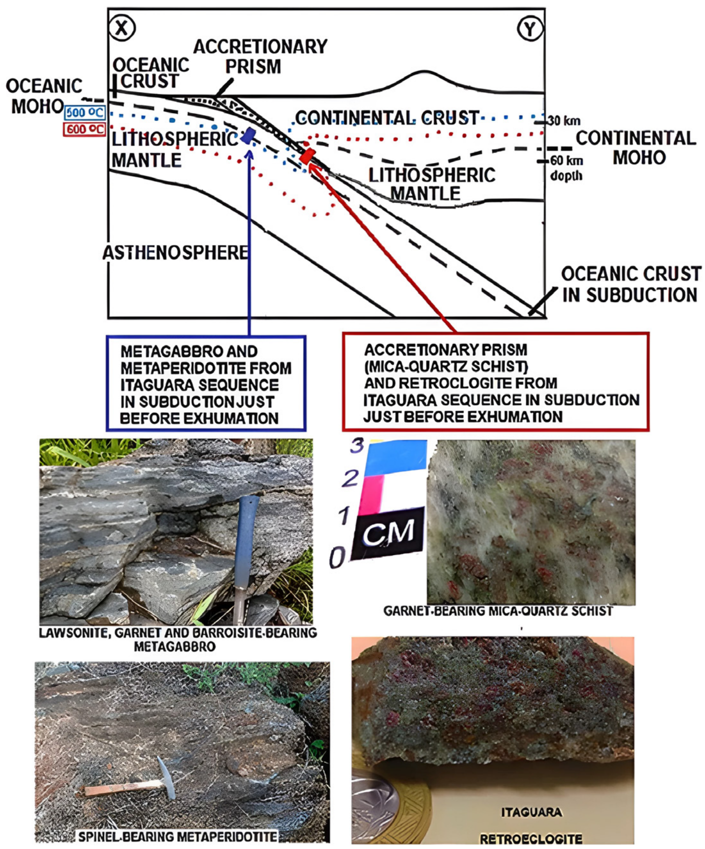

Figure 13. The ca. 2.13 Ga subduction setting envisaged for the Itaguara Sequence just before tectonic exhumation related to the ca. 2.1 Ga collision between Archean Divinópolis (X—not shown in the figure) and Campo Belo/Bonfim (Y) complexes.

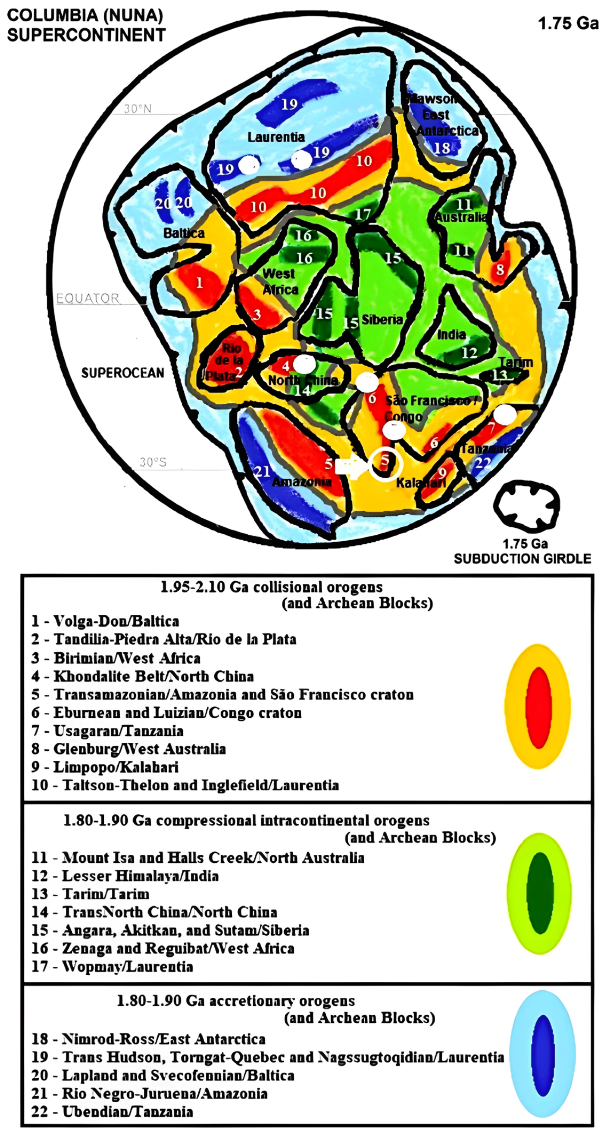

Figure 14. Distribution of concentric collisional (1.95–2.10 Ga), accretionary and compressional intracontinental (1.80–1.90 Ga) orogens and undiscriminating Archean blocks on 1.75 Ga Columbia (Nuna) supercontinent. White circles represent locations of 2.10–1.90 Ga retroeclogites preserved inside contemporary accretionary and collisional orogens. White arrow indicates the location of the IS (open white circle), with ~2.1 Ga retroeclogite and probable blueschist investigated herein (modified from Chaves [74], permitted reproduction—copyright Elsevier).

Funding

This research received no external funding.

Acknowledgments

Author thanks to CNPq (Brazilian science and technology agency) for the research productivity grant, anonymous reviewers for constructive comments, Roberto Pereira and Cristiano Lana for support on titanite U-Pb data, and Elsevier for permission to reproduce Figures 1, 2 and 14, taken from references [5] and [74] below.

Data Availability Statement

The corresponding author guarantees that the data used to carry out this study are integrally published in the paper.

Conflict of Interest

The author disclosed no conflicts of interest.

References

[1] Maruyama, S., Liou, J.G., Terabayashi, M., 1996. Blueschists and eclogites of the world and their exhumation. International Geology Review. 38, 485–594.
DOI: https://doi.org/10.1080/00206819709465347

[2] Agard, P., Yamato, P., Jolivet, L., et al., 2009. Exhumation of oceanic blueschists and eclogites in subduction zones: Timing and mechanisms. Earth-Science Reviews. 92, 53–79.
DOI: https://doi.org/10.1016/j.earscirev.2008.11.002

[3] Sanità, E., Di Rosa, M., Lardeaux, J.-M., et al., 2022. The Moglio-Testico Unit (Ligurian Alps, Italy) as subducted metamorphic oceanic fragment: stratigraphic, structural and metamorphic constraints. Minerals. 12(11), 1343.
DOI: https://doi.org/10.3390/min12111343

[4] Palin, R.M., Santosh, M., 2021. Plate tectonics: what, where, why, and when? Gondwana Research. 100, 3–24.
DOI: https://doi.org/10.1016/j.gr.2020.11.001

[5] Chaves, A.O., Goulart, L.E.A., Coelho, R.M., et al., 2019. High-pressure eclogite facies metamorphism and decompression melting recorded in paleoproterozoic accretionary wedge adjacent to probable ophiolite from Itaguara (southern São Francisco Craton—Brazil). Journal of South American Earth Sciences. 94, 102226.
DOI: https://doi.org/10.1016/j.jsames.2019.102226

[6] Chaves, A.O., Coelho, R.M., 2020. Reply to "Comments to high-pressure eclogite facies metamorphism and decompression melting recorded in Paleoproterozoic accretionary wedge adjacent to probable ophiolite from Itaguara (southern São Francisco Craton—Brazil)". Journal of South American Earth Sciences. 99, 102510.

DOI: https://doi.org/10.1016/j.jsames.2020.102510

[7] Aguilar, C., Alkmim, F.F., Lana, C. et al., 2017. Palaeoproterozoic assembly of the São Francisco craton, SE Brazil: new insights from U-Pb titanite and monazite dating. Precambrian Research. 289, 95–115.
DOI: https://doi.org/10.1016/j.precamres.2016.12.001

[8] Miranda, D.A., Chaves, A.O., Dussin, I.A., et al., 2020. Paleoproterozoic khondalites in Brazil: a case study of metamorphism and anatexis in khondalites from Itapecerica supracrustal succession of the southern São Francisco Craton. International Geology Review. 64(4), 397–421.
DOI: https://doi.org/10.1080/00206814.2020.1716273

[9] Chaves, A.O., Porcher, C.C., 2020. Petrology, geochemistry and Sm-Nd systematics of the Paleoproterozoic Itaguara retroeclogite from São Francisco/Congo Craton: one of the oldest records of the modern-style plate tectonics. Gondwana Research. 87, 224–237.
DOI: https://doi.org/10.1016/j.gr.2020.06.014

[10] Setiawan, N.I., Osanai, Y., Nakano, N., et al., 2015. Metamorphic evolution of garnet bearing epidote-barroisite schist from the Meratus Complex in South Kalimantan, Indonesia. Indonesian Journal on Geoscience. 2(3), 139–156.
DOI: https://doi.org/10.17014/ijog.2.3.139-156

[11] Kato, R., Hirajima, T., 2017. Petrology and possible significance of barroisite–bearing metabasite from the Kebara Formation in NW Kii Peninsula. Journal of Mineralogical and Petrological Sciences. 112, 40–45.
DOI: https://doi.org/10.2465/jmps.160719a

[12] Goulart, L.E.A., Carneiro, M.A., 2010. Paleoproterozoic mafic-ultramafic magmatism in Southern São Francisco craton: the Itaguara layered sequence. 45° Congresso Brasileiro de Geologia, Sociedade Brasileira de Geologia, Belém, Anais (in Portuguese).

[13] Whitney, D.L., Fornash, K.F., Kang, P., et al., 2020. Lawsonite composition and zoning as tracers of subduction processes: A global review. Lithos. 370–371, 105636.
DOI: https://doi.org/10.1016/j.lithos.2020.105636

[14] Tsujimori, T., Ernst, W.G., 2014. Lawsonite blueschists and lawsonite eclogites as proxies for palaeo-subduction zone processes: A review. Journal of Metamorphic Geology. 32(5), 437–454.
DOI: https://doi.org/10.1111/jmg.12057

[15] Almeida, F.F.M., Hasui, Y., Brito Neves, B.B. et al., 1981. Brazilian structural provinces: An introduction. Earth Science Reviews. 17(1–2), 1–29.
DOI: https://doi.org/10.1016/0012-8252(81)90003-9

[16] Pedrosa Soares, A.C., Noce, C.M., Wiedemann, C.M., et al., 2001. The Araçuaí-West-Congo orogen in Brazil: an overview of a confined orogen formed during Gondwanaland assembly. Precambrian Research. 110(1–4), 307–323.
DOI: https://doi.org/10.1016/S0301-9268(01)00174-7

[17] Pimentel, M., Dardenne, M., Fuck, R., et al., 2001. Nd isotopes and the provenance of detrital sediments of the Neoproterozoic Brasılia Belt, central Brazil. Journal of South American Earth Sciences. 14(6), 571–585.
DOI: https://doi.org/10.1016/S0895-9811(01)00041-4

[18] Teixeira, W., Carneiro, M.A., Noce, C.M., et al., 1996. Pb, Sr and Nd isotope constraints on the Archean evolution of the gneissic-granitoid in the southern São Francisco Craton, Brazil. Precambrian Research. 78(1–3), 151–164.
DOI: https://doi.org/10.1016/0301-9268(95)00075-5

[19] Dorr, J.V.N., 1969. Physiographic, stratigraphic and structural development of Quadrilatero Ferrifero, Minas Gerais, Brazil. USGS/DNPM Professional paper. 641-A, 110.
DOI: https://doi.org/10.3133/pp641A

[20] Baltazar, O.F., Zucchetti, M., 2007. Lithofacies associations and structural evolution of the Archean Rio das Velhas greenstone belt, Quadrilátero Ferrífero, Brazil: a review of the setting of gold deposits. Ore Geology Reviews. 32, 471–499.
DOI: https://doi.org/10.1016/j.oregeorev.2005.03.021

[21] Machado, N., Schrank, A., Noce, C.M., et al., 1996. Ages of detrital zircon from Archean-Paleoproterozoic sequences: implications for Greenstone Belt setting and evolution of a Transamazonian foreland basin in Quadrilátero Ferrífero, southeast Brazil. Earth and Planetary Science Letters. 141, 259–276.
DOI: https://doi.org/10.1016/0012-821X(96)00054-4

[22] Machado Filho, L., Ribeiro, M.W., Gonzalez, S.R., et al., 1983. SF 23/24 Sheets, Rio de Janeiro/Vitoria: geology, geomorphology, pedology, vegetation, potential use of the land/RADAMBRASIL Project [v. 32]. O Pro-

jeto: Rio de Janeiro/Vitória, 32. pp 36–45. Available from: https://biblioteca.ibge.gov.br/biblioteca-catalogo?id=217129&view=detalhes (in Portuguese).

[23] Lana, C., Alkmim, F.F., Armstrong, R., et al., 2013. The ancestry and magmatic evolution of Archaean TTG rocks of the Quadrilátero Ferrífero province, southeast Brazil. Precambrian Research. 231, 157–173.
DOI: https://doi.org/10.1016/j.precamres.2013.03.008

[24] Romano, R., Lana, C., Alkimim, F.F., et al., 2013. Stabilization of the southern portion of the Sao Francisco Craton, SE Brazil, through a long-lived period of potassic magmatism. Precambrian Research. 224, 143–159.

[25] Farina, F., Albert, C., Dopico, C.M., et al., 2016. The Archean-Paleoproterozoic evolution of the Quadrilátero Ferrífero (Brasil): Current models and open questions. Journal of South American Earth Sciences. 68, 4–21.
DOI: https://doi.org/10.1016/j.jsames.2015.10.015

[26] Moreira, H., Lana, C., Nalini, H.A., 2016. The detrital zircon record of an Archaean convergent basin in the Southern São Francisco Craton, Brazil. Precambrian Research. 275, 84–99.
DOI: https://doi.org/10.1016/j.precamres.2015.12.015

[27] CPRM – Brazilian Geological Survey and CODEMIG, Companhia de Desenvolvimento Econômico de Minas Gerais, 2014. Mapa Geológico do Estado de Minas Gerais. Escala 1:1000000 DVD-rom. Available from: https://rigeo.cprm.gov.br/jspui/handle/doc/20786/ (in Portuguese).

[28] Teixeira, W., Ávila, C.A., Dussin, I.A., et al., 2015. A juvenile accretion episode (2.35–2.32 Ga) in the Mineiro belt and its role to the Minas accretionary orogeny: zircon U-Pb-Hf and geochemical evidences. Precambrian Research. 256, 148–169.
DOI: https://doi.org/10.1016/j.precamres.2014.11.009

[29] Noce, C.M., Machado, N., Teixeira, W., 1998. U-Pb geochronology of gneisses and granitoids in the Quadrilátero Ferrífero (southern São Francisco Craton): age constraints for Archean and Paleoproterozoic magmatism and metamorphism. Brazilian Journal of Geology. 28, 95–102.
DOI: https://doi.org/10.25249/0375-7536.199895102

[30] Ávila, C.A., Teixeira, W., Bongiolo, E.M., et al., 2014. Rhyacian evolution of subvolcanic and metasedimentary rocks of the southern segment of the Mineiro belt, Sao Francisco Craton, Brazil. Precambrian Research. 243, 221–251.
DOI: https://doi.org/10.1016/j.precamres.2013.12.028

[31] Noce, C.M., Pedrosa Soares, A.C., Silva, L.C., et al., 2007. Evolution of polycyclic basement complexes in the Araçuaí Orogen, based on U-Pb SHRIMP data: Implications for Brazil-Africa links in Paleoproterozoic time. Precambrian Research. 159, 60–78.
DOI: https://doi.org/10.1016/j.precamres.2007.06.001

[32] Alkmim, F.F., Marshak, S., 1998. Transamazonian Orogeny in the Southern São Francisco Craton Region, Minas Gerais, Brazil: Evidence for Paleoproterozoic collision and collapse in the Quadrilátero Ferrífero. Precambrian Research. 90, 29–58.
DOI: https://doi.org/10.1016/S0301-9268(98)00032-1

[33] Campos, J.C.S., Carneiro, M.A., 2008. Neoarchean and Paleoproterozoic granitoids marginal to the Jeceaba-Bom Sucesso lineament (SE border of the southern São Francisco Craton): genesis and tectonic evolution. Journal of South American Earth Sciences. 26, 463–484.
DOI: https://doi.org/10.1016/j.jsames.2008.09.002

[34] Carvalho, B.B., Janasi, V.A., Sawyer, E.W., 2017. Evidence for Paleoproterozoic anatexis and crustal reworking of Archean crust in the São Francisco Craton, Brazil: A dating and isotopic study of the Kinawa migmatite. Precambrian Research. 291, 98–118.
DOI: https://doi.org/10.1016/j.precamres.2017.01.019

[35] Chaves, A.O., Campello, M.S., Pedrosa Soares, A.C., 2015. Monazite U-Th-PbT age of the sillimanite-cordierite-garnet-biotite gneiss from Itapecerica (MG) and the actuation of the Rhyacian/Orosirian orogeny in the inner part of the southern São Francisco Craton. Geociências. 34, 324–334. Available from: https://www.revistageociencias.com.br/geociencias-arquivos/34/volume34_3_files/34-3-artigo-01.pdf (in Portuguese).

[36] Chaves, A.O., Pires, A.C.C., Brasil, M.F.A., 2021. New knowledge update on mafic dyke swarms of Minas Gerais (Brazil): Fragments of ancient large igneous provinces highlighted by aeromagnetometry. Brazilian Journal of Geophysics. 39(2), 227–235.
DOI: http://dx.doi.org/10.22564/rbgf.v39i3.2096

[37] Goulart, L.E.A., Carneiro, M.A., 2008. General characteristics and lithogeochemistry of the Itaguara layered (ultramafic-mafic) sequence, southern São Francisco Craton. Geochimica Brasiliensis. 22, 045–072.

[38] Pinheiro, S.O., Nilson, A.A., 2000. Metakomatiitic and meta-ultramafic rocks from the Rio Manso region, Minas Gerais: geology, textures and metamorphism. Revista Brasileira de Geociências. 30, 417–419.

[39] de Capitani, C., Petrakakis, K., 2010. The computation of equilibrium assemblage diagrams with Theriak/Domino software. American Mineralogist. 95, 1006-1016.
DOI: https://doi.org/10.2138/am.2010.3354

[40] Holland, T.J.B., Powell, R., 2011. An improved and extended internally consistent thermodynamic dataset for phases of petrological interest, involving a new equation of state for solids. Journal of Metamorphic Geology. 29(3), 333–383.
DOI: https://doi.org/10.1111/j.1525-1314.2010.00923.x

[41] Van Achterbergh, E., Ryan, C.G., Jackson, S.E., et al., 2001. Data reduction software for LA-ICP-MS: Appendix. In: Sylvester P.J. (ed.). Mineralogical Association of Canada Short Course Series. 29, 239–243.

[42] Griffin, W.L., Powell, W.J., Pearson, N.J., et al., 2008. Glitter: Data reduction software for laser ablation ICP-MS. In: Sylvester P.J. (ed.), Laser ablation ICP-MS in the Earth sciences: Current practices and outstanding issues. Mineralogical Association of Canada Short Course Series. 40, 308–311.

[43] Gerdes, A., Zeh, A., 2006. Combined U–Pb and Hf isotope LA-(MC-)ICP-MS analyses of detrital zircons: Comparison with SHRIMP and new constraints for the provenance and age of an Armorican metasediment in central Germany. Earth and Planetary Science Letters. 249, 47–61.
DOI: https://doi.org/10.1016/j.epsl.2006.06.039

[44] Gerdes, A., Zeh, A,, 2009. Zircon formation versus zircon alteration—New insights from combined U-Pb and Lu-Hf in-situ LA-ICP-MS analyses of Archaean zircons from the Limpopo Belt. Chemical Geology. 261, 230–243.
DOI: https://doi.org/10.1016/j.chemgeo.2008.03.005

[45] Chew, D.M., Petrus, J.A., Kamber, B.S., 2014. U-Pb LA-ICP-MS dating using accessory mineral standards with variable Pbc. Chemical Geology. 363, 185–199.
DOI: http://dx.doi.org/10.1016/j.chemgeo.2013.11.006

[46] Ludwig, K.R., 2003. Isoplot 3.00: A geochronological toolkit for Microsoft Excel. Berkeley Geochronology Center, Berkeley, 70.

[47] Mazoz, A., Gonçalves, G.O., Lana, C., et al., 2022. Khan river and bear lake: two natural titanite reference materials for high-spatial resolution U-Pb microanalysis. Geostandards and Geoanalytical Research. 46(4), 701–733.
DOI: https://doi.org/10.1111/ggr.12444

[48] Whitney, D.L., Evans, B.W., 2010. Abbreviations for names of rock-forming minerals. American Mineralogist. 95, 185–187.
DOI: https://doi.org/10.2138/am.2010.3371

[49] Leake, B.E., Woolley, A.R., Arps, C.E.S., et al., 1997. Nomenclature of amphiboles: report of the subcommittee on amphiboles of the international mineralogical commission on new minerals and mineral names. Mineralogical Magazine. 61, 295–310.
DOI: https://doi.org/10.1180/minmag.1997.061.405.13

[50] Winter, J.D., 2014. Principles of igneous and metamorphic petrology, 2 ed. Pearson Education Limited: Harlow. pp. 738. Available from: https://www.whitman.edu/geology/winter/Winter_Principles%20of%20Igneous%20and%20Metamorphic%20Petrology%20by%20JOHN%20D.%20WINTER-1.pdf

[51] Ravna, E.K., 2000. Distribution of Fe^{2+} and Mg between coexisting garnet and hornblende in synthetic and natural systems: an empirical calibration of the garnet-hornblende Fe–Mg geothermometer. Lithos. 53, 265–277.
DOI: https://doi.org/10.1016/S0024-4937(00)00029-3

[52] Palin, R.M., Santosh, M., Cao, W., et al., 2020. Secular change and the onset of plate tectonics on Earth. Earth Science Reviews. 207, 103172.
DOI: https://doi.org/10.1016/j.earscirev.2020.103172

[53] Kamzolkin, V.A., Ivanov, S.D., Konilov, A.N., 2016. Empirical phengite geobarometer: Background, calibration, and application. Geology of Ore Deposits. 58(8), 613–622.
DOI: https://doi.org/10.1134/S1075701516080092

[54] Xia, L., Li, X., 2019. Basalt geochemistry as a diagnostic indicator of tectonic setting. Gondwana Research. 65, 43–67.
DOI: https://doi.org/10.1016/j.gr.2018.08.006

[55] Irvine, T.N., Baragar, W.R.A., 1971. A guide to the chemical classification of common volcanic rocks. Canadian Journal of Earth Sciences. 8, 523–548. DOI: https://doi.org/10.1139/e71-055

[56] Pearce, J.A., Cann, J.R., 1973. Tectonic setting of basic volcanic rocks determined using trace element analyses. Earth and Planetary Science Letters. 19, 290–300. DOI: https://doi.org/10.1016/0012-821X(73)90129-5

[57] Sun, S.S., McDonough, W.F., 1989. Chemical and isotopic systematics of oceanic basalts: Implications for mantle composition and processes. Magmatism in the Ocean Basins. 42, 313–345. DOI: https://doi.org/10.1144/GSL.SP.1989.042.01.19

[58] Liang, J.L., Ding, X., Sun, X.M., et al., 2009. Nb/Ta fractionation observed in eclogites from the Chinese Continental Scientific Drilling Project. Chemical Geology. 268, 27–40. DOI: https://doi.org/10.1016/j.chemgeo.2009.07.006

[59] Hernández-Uribe, D., Palin, R.M., 2019. A revised petrological model for subducted oceanic crust: Insights from phase equilibrium modeling. Journal of Metamorphic Geology. 37(6), 745–768. DOI: https://doi.org/10.1111/jmg.12483

[60] Pearce, J.A., 2008. Geochemical fingerprinting of oceanic basalts with applications to ophiolite classification and the search for Archean oceanic crust. Lithos. 100, 14–48. DOI: https://doi.org/10.1016/j.lithos.2007.06.016

[61] Clarke, G.L., Powell, R., Fitzherbert, J.A., 2006. The lawsonite paradox: a comparison of field evidence and mineral equilibria modelling. Journal of Metamorphic Geology. 24, 715–725. DOI: https://doi.org/10.1111/j.1525-1314.2006.00664.x

[62] Zack, T., Rivers, T., Brumm, R., et al., 2004. Cold subduction of oceanic crust: Implications from a lawsonite eclogite from the Dominican Republic. European Journal of Mineralogy. 16, 909–916.

[63] Chen, Y., Ye, K., Wu, T.F., et al., 2013. Exhumation of oceanic eclogites: thermodynamic constraints on pressure, temperature, bulk composition and density. Journal of Metamorphic Geology. 31, 549–570. DOI: https://doi.org/10.1111/jmg.12033

[64] Chaves, A.O., Dutra, A.C.O.M., 2020. Collisional event and thermal events of Proterozoic age recorded by monazite included in corundum from Itaguara (southern São Francisco Craton, Brazil). Comunicações Geológicas. 107(1), 5–12. Available from: https://repositorio.lneg.pt/bitstream/10400.9/3568/1/evento-colisional-e-eventos-t%C3%A9rmicos-proteroz%C3%B3icos-registados-2020.pdf (in Portuguese).

[65] Stern, R.J., Tsujimori, T., Harlow, G.E., et al., 2013. Plate tectonic gemstones. Geology. 41, 723–726. DOI: https://doi.org/10.1130/G34204.1

[66] Brown, M., Johnson, T., 2019. Metamorphism and the evolution of subduction on Earth. American Mineralogist. 104, 1065–1082. DOI: https://doi.org/10.2138/am-2019-6956

[67] Möller, A., Appel, P., Mezger, K., et al., 1995. Evidence for a 2 Ga subduction zone: Eclogites in the Usagaran belt of Tanzania. Geology. 23(12), 1067–1070. DOI: https://doi.org/10.1130/0091-7613(1995)023<1067:EFAGSZ>2.3.CO;2

[68] Zhao, G., Cawood, P.A., Wilde, S.A., et al., 2001. High-pressure granulites (retrograded eclogites) from the Hengshan Complex, North China Craton: petrology and tectonic implications. Journal of Petrology. 42(6), 1141–1170. DOI: https://doi.org/10.1093/petrology/42.6.1141

[69] Glassley, W.E., Korstgard, J.A., Storensen, K., et al., 2014. A new UHP metamorphic complex in the ~1.8 Ga Nagssugtoqidian orogen of west Greenland. American Mineralogist. 99, 1315–1334. DOI: https://doi.org/10.2138/am.2014.4726

[70] Weller, O., St-Onge, M., 2017. Record of modern-style plate tectonics in the Palaeoproterozoic Trans-Hudson orogen. Nature Geoscience. 10, 305–311. DOI: https://doi.org/10.1038/ngeo2904

[71] François, C., Debaille, V., Paquette, J.L., et al., 2018. The earliest evidence for modern-style plate tectonics recorded by HP–LT metamorphism in the Paleoproterozoic of the Democratic Republic of the Congo. Scientific Reports. 8, 15452. DOI: https://doi.org/10.1038/s41598-018-33823-y

[72] Loose, D., Schenk, V., 2018. 2.09 Ga old eclogites in the Eburnian-Transamazonian orogen of southern Cameroon: significance for Palaeoproterozoic plate tectonics. Precambrian Research. 304, 1–11. DOI: https://doi.org/10.1016/j.precamres.2017.10.018

[73] Bouyo, M.H., Penaye, J., Mouri, H., et al., 2019. Eclogite facies metabasites from the Paleoproterozoic Nyong Group, SW Cameroon: Mineralogical evidence and implications for a high-pressure

metamorphism related to a subduction zone at the NW margin of the Archean Congo Craton. Journal of African Earth Sciences. 149, 215–234. DOI: https://doi.org/10.1016/j.jafrearsci.2018.08.010

[74] Chaves, A.O., 2021. Columbia (Nuna) supercontinent with external subduction girdle and concentric accretionary, collisional and intracontinental orogens permeated by large igneous provinces and rifts. Precambrian Research. 352, 106017. DOI: https://doi.org/10.1016/j.precamres.2020.106017